A model for turbulent hydraulic fracture and application to crack propagation at glacier beds

Victor C. Tsai[1,2] and James R. Rice[3]

[1] Glaciological observations of under-flooding suggest that fluid-induced hydraulic fracture of an ice sheet from its bed sometimes occurs quickly, possibly driven by turbulently flowing water in a broad sheet flow. Taking the approximation of a fully turbulent flow into an elastic ice medium with small fracture toughness, we derive an approximate expression for the crack-tip speed, opening displacement and pressure profile. We accomplish this by first showing that a Manning-Strickler channel model for resistance to turbulent flow leads to a mathematical structure somewhat similar to that for resistance to laminar flow of a power law viscous fluid. We then adapt the plane-strain asymptotic crack solution of Desroches et al. (1994) and the power law self-similar solution of Adachi and Detournay (2002) for that case to calculate the desired quantities. The speed of crack growth is shown to scale as the overpressure (in excess of ice overburden) to the power 7/6, inversely as ice elastic modulus to the power 2/3, and as the ratio of crack length to wall roughness scale to the power 1/6. We tentatively apply our model by choosing parameter values thought appropriate for a basal crack driven by the rapid drainage of a surface meltwater lake near the margin of the Greenland Ice Sheet. Making various approximations perhaps relevant to this setting, we estimate fluid inflow rate to the basal fracture and vertical and horizontal surface displacements and find order-of-magnitude agreement with observations by Das et al. (2008) associated with lake drainage. Finally, we discuss how these preliminary estimates could be improved.

1. Introduction

[2] Hydraulic fracture has, since the 1940's, been a subject of great interest in the context of inducing production from oil and gas wells (see, e.g., *Mendelsohn* [1984] for a review). More recently, the topic has been explored in depth theoretically [*Lister*, 1990; *Desroches et al.*, 1994; *Dyskin et al.*, 2000; *Adachi and Detournay*, 2002; *Savitski and Detournay*, 2002; *Detournay*, 2004; *Garagash and Detournay*, 2005; *Roper and Lister*, 2007], in the context of magma-driven cracking [*Rubin*, 1995], and in the context of water-aided vertical crevassing in glaciers [*Weertman*, 1971a, 1973; *Smith*, 1976; *van der Veen*, 1998; *Kenneally*, 2003; *Alley et al.*, 2005; *van der Veen*, 2007; *Krawczynski et al.*, 2009]. These works have successfully applied the results of linear elastic fracture mechanics (LEFM) with different assumptions of fluid-related boundary conditions on the crack face. The boundary conditions used have ranged from the simple quasi-static loading case common in the glaciological literature [*Weertman*, 1973; *Smith*, 1976; *van der Veen*, 1998, 2007; *Krawczynski et al.*, 2009] to the more complex but realistic case for which the pressure distribution within the crack is determined along with the crack separation as a coupled fluid-flow/elasticity problem [*Desroches et al.*, 1994; *Adachi and Detournay*, 2002].

[3] As interest regarding the very short timescale behavior of glaciers intensifies [*Bindschadler et al.*, 2003; *Ekstrom et al.*, 2006; *Das et al.*, 2008; *Wiens et al.*, 2008], it will become of paramount importance to understand the fracture process in glaciers since it influences fundamental aspects of glacial dynamics, including flow speeds, calving behavior, and stability of the ice sheet [e.g., *Zwally et al.*, 2002; *Kenneally*, 2003; *Joughin et al.*, 2008; *Tsai et al.*, 2008]. The current literature on the processes leading to crevasse extension to depth is fairly small (see previous paragraph) but there is agreement that the presence of liquid water greatly enhances the ability for crevasses to quickly grow, become macroscopic and affect large-scale features of ice sheets. Recent observations by *Das et al.* [2008] of drainage of a large supraglacial meltwater lake into, and presumably to the bed of, the Greenland Ice Sheet within a timespan of a few hours show that water flow rates into crevasses can be

[1]Department of Earth and Planetary Sciences, Harvard University, Cambridge, Massachusetts, USA.
[2]Now at U.S. Geological Survey, Golden, Colorado, USA.
[3]Department of Earth and Planetary Sciences and School of Engineering and Applied Sciences, Harvard University, Cambridge, Massachusetts, USA.
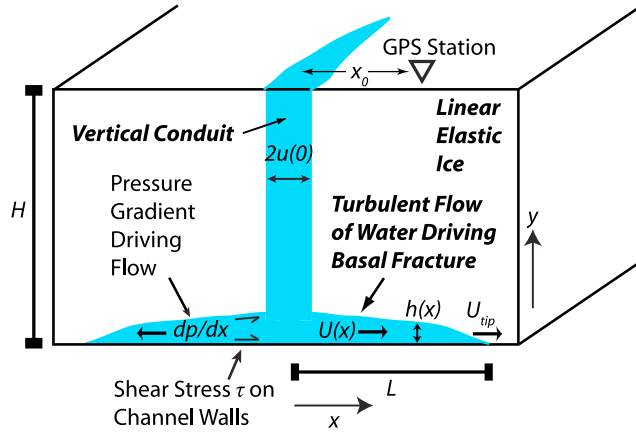
Figure 1. Schematic of the model. A vertical conduit (crack) of height H connects a surficial lake with a basal crack, which is driven open by turbulent flow of water through the crack system. In the model solutions, a 2D plane strain problem is solved for simplicity, effectively assuming the surficial crack is infinitely long. However, in applying the results, we assume the third dimension length scales with L, the half-length of the basal crack. The variables are described in the text.

very fast. They measured the volume of initial lake water to be $V_0 \approx 4.4 \cdot 10^7$ m^3, and found that it drained completely within a timescale of $T \approx 2$ hours, implying an average drainage rate of $8.7 \cdot 10^3$ m^3/s. They further observed a crack-like surface feature (with length $L_c \approx 3$ km, approximately equal to the lake dimension), and had a GPS station nearby that showed meter-scale surface displacements associated with the drainage event. A crude estimate of the Reynolds number, $\Re$, for this flow can then be made by assuming that V_0 drains into a basal crack system of lateral dimension L_c (in the out-of-page direction of Figure 1) over time T, leading to an average velocity of $V_0/(L_c h_0 T)$, where h_0 is a representative opening of the crack. With water density of $\rho \approx 10^3$ kg/m^3 and viscosity of $\eta \approx 2 \cdot 10^{-3}$ Pa s, this crude estimate yields a Reynolds number of $\Re = \rho V_0/(L_c T \eta) \approx 10^6$, which is well within the fully turbulent regime. These observations therefore motivate the present work, in which we consider the turbulent flow of draining surface water as causing the opening of a basal crack within a linear-elastic ice medium. This corresponds to under-flooding as a rapid sheet flow, e.g., as considered by *Roberts* [2005] and *Flowers et al.* [2004], as opposed to a wholly channelized flow [*Rothlisberger*, 1972; *Clarke*, 1996]. Although these approximations of fully turbulent sheet flow in a fracture within a purely elastic medium are clearly short-timescale end-member cases of a more general scenario, they are reasonable and allow for considerable simplification of the mathematical analysis.

[4] In Section 2, we present solutions for the crack-tip speeds, pressure profiles and displacement profiles from an approximate interpretation of a steady state crack growth analysis and from an exact self-similar analysis. In Section 3, we then tentatively apply these results to glacial crack propagation, compare our results to the recent observations

of meter-scale ice sheet displacements associated with rapid drainage by *Das et al.* [2008], and find order-of-magnitude agreement between model and observation. Although we do not explicitly consider the case of jökulhlaup (subglacial outburst flood) initiation, our model applies to the relatively early (but post-nucleation) growth stages of these events to the extent that jökulhlaup initiation can be thought of as the crack-like growth of a subglacial lake under excess water pressure [see, e.g., *Roberts*, 2005]. Traditional thermodynamic treatments of the jökulhlaup problem [e.g., *Nye*, 1976; *Ng and Bjornsson*, 2003] would apply only after this initial stage of growth is over. The model may also have some relevance to satellite-inferred fluid interchanges between sub-glacial lakes documented by *Fricker et al.* [2007].

2. Model Setup: Turbulent Hydraulic Fracture

[5] In this section, we consider a crack within an elastic medium driven open by the turbulent flow of water through the crack. To model this, we adapt various power law viscous-flow crack solutions [*Desroches et al.*, 1994; *Adachi and Detournay*, 2002] for use in our case with a Manning-Strickler channel model [*Manning*, 1891; *Strickler*, 1923, 1981] for wall shear resistance to turbulent flow [see, e.g., *Rouse*, 1955]. The geometry first considered here is that of a plane strain horizontal crack of length $2L$ within an impermeable linearly-elastic medium, located at a depth H beneath the surface. The crack opening profile is given by $h(x)$ for $-L < x < L$ (see Figure 1).

2.1. Manning Turbulent Friction

[6] For flow through a channel of height h, the average shear stress τ on the channel walls is given by

$$2\tau \equiv \frac{f}{4}\rho U^2 = -h\frac{\partial p}{\partial x}, \qquad (1)$$

for $0 < x < L$, where h is the local channel height, $\partial p/\partial x$ is the pressure gradient (see Figure 1), f is the commonly-used "Darcy-Weisbach" friction factor, ρ is the fluid density, U is the fluid velocity averaged across h, and the sign in Equation (1) is reversed when $x < 0$. In order to use this relationship between the velocity and pressure gradient in the crack solution, we must estimate f. Here, we assume that the flow is fully turbulent so that f is given by the Gauckler-Manning-Strickler approximation [*Manning*, 1891; *Strickler*, 1923, 1981]

$$f = 0.113\left(\frac{k}{R_h}\right)^{1/3} = f_0\left(\frac{k}{h}\right)^{1/3} = 0.143\left(\frac{k}{h}\right)^{1/3}, \qquad (2)$$

where $R_h = h/2$ is the hydraulic radius and k is the Nikuradse channel wall roughness height [*Rubin and Atkinson*, 2001]. When the two walls have different roughness, it is appropriate to interpret $k^{1/3}$ as the average of $k^{1/3}$ for the upper and lower walls. This expression, Equation (2), is known to be approximately valid when the Reynolds number $\Re$ is sufficiently large, $\Re \gtrsim 10^5$ [see e.g., *Rubin and Atkinson*, 2001; *Gioia and Chakraborty*, 2006; *White*, 2008]. This inequality is verified in Section 3 for the case of interest.
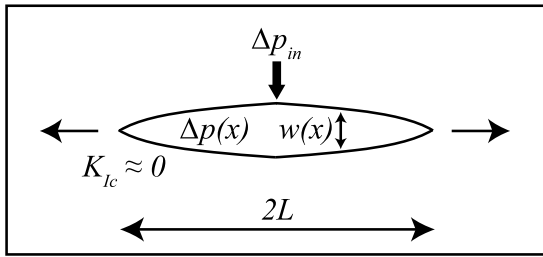
Figure 2. Schematic for stress calculation. The actual crack opening, h, between ice and bedrock is assumed to be ξw, where w is the modeled full width for an identically loaded crack in a homogeneous ice body and ξ is given by Equation (8). The excess pressure at $x = 0$ is assumed to be given by Δp_{in} and the fracture toughness K_{Ic} is assumed negligible.

This scaling is also equivalent to the commonly used Manning approximation

$$U_{Manning} = \frac{1}{n} R_h^{2/3} S^{1/2}. \tag{3}$$

Here, n is the Manning roughness parameter,

$$S = -\frac{1}{\rho g} \frac{\partial p}{\partial x} \left(= \frac{2\tau}{\rho g h} \right) \tag{4}$$

is the negative hydraulic head gradient (positive in the direction of flow) [e.g., *Rouse*, 1955], and g is gravitational acceleration. In Equations (1) and (4), we have assumed that $\rho DU/Dt$ is of small magnitude compared to $\partial p/\partial x$, as will be checked subsequently, and that the gravity forcing due to slope of the flow channel is likewise negligible compared to the pressure gradient (otherwise, the slope is added to the definition of S). The value of f_0 used in Equation (2) is equivalent to setting

$$n = \left(0.0380 \text{ s m}^{-1/2} \right) \cdot k^{1/6} \tag{5}$$

(e.g., $n = 0.018$ s m$^{-1/3}$ when $k = 1$ cm). Our results turn out to be very weakly dependent on the size of k.

[7] Substituting Equation (2) into Equation (1) gives

$$-\frac{\partial p}{\partial x} = \frac{f_0}{4} \rho U^2 \frac{k^{1/3}}{h^{4/3}} = 0.0357 \rho U^2 \frac{k^{1/3}}{h^{4/3}}. \tag{6}$$

The turbulent Manning-Strickler scaling therefore provides one relationship between the local pressure gradient $\partial p(x, t)/\partial x$, fluid velocity $U(x, t)$, and channel opening $h(x, t)$.

2.2. Basic Equations Governing Turbulent Hydraulic Fracture

[8] The problem of a fracture driven through an impermeable linear elastic body by injection of a power law viscous fluid has been studied by a number of authors. Key results include an analytical near-tip solution in plane strain [*Desroches et al.*, 1994], a (numerical) self-similar solution for a plane strain fracture of finite length [*Adachi and Detournay*, 2002], and a solution for a penny-shaped (cylindrically symmetric) fracture [*Savitski and Detournay*, 2002]. Here, we use an approach analogous to these power law solutions but modified to allow for the turbulent

flow condition of Section 2.1. In so doing, we find it convenient to consider the related problem of a plane strain crack in an imagined homogeneous medium (as shown in Figure 2) with elastic properties that are those of ice. For this model crack, we assume there to be three fundamental considerations that relate the crack opening displacement profile $w(x, t)$, the crack pressure profile $p(x, t)$, and the crack fluid velocity profile $U(x, t)$. (The relation of w, the crack opening in an imagined homogeneous ice material, to h, the channel width at the glacier interface with its bed, is discussed below; we will choose h proportional to w with a coefficient of proportionality ξ that is rationalized in Appendix A of Text S1.[1]) Elasticity theory provides one equation, the turbulent scaling of Equation (6) provides another, and fluid mass conservation provides the third equation. As in the work of *Desroches et al.* [1994] and *Adachi and Detournay* [2002], we solve the case for negligible fracture energy (i.e. negligible energy required to add new crack area). As will be shown in Section 3, with estimates of ice fracture toughness from *Ashby* [1989] (see also *Schulson and Duval* [2009, p. 208]), *Fischer et al.* [1995], and *Rist et al.* [1999] showing $K_{Ic} \approx 0.1$–0.2 MPa m$^{1/2}$, and guidelines like those of *Savitski and Detournay* [2002] and *Bunger and Detournay* [2008], this approximation is reasonable for the glacial application considered.

[9] For a crack (of length $2L$) in an infinite, homogeneous elastic medium, it is well known that a singular integral equation [*Muskhelishvili*, 1953; *Bilby et al.*, 1963] relates $w(x, t)$ and $p(x, t)$. In the following, we assume that there exists a local hydrostatic ice overburden pressure given by σ_0 so that the pressure causing crack opening is given by the excess pressure $\Delta p(x, t) \equiv p(x, t) - \sigma_0$. The integral equation can then be represented as

$$\Delta p(x, t) \equiv p - \sigma_0 = \frac{E'}{4\pi} \int_{-L}^{L} \frac{\partial w(s, t)}{\partial s} \frac{ds}{x - s}, \tag{7}$$

where $E' = E/(1 - \nu^2)$, E is Young's modulus, and ν is Poisson's ratio. For the crack of interest at a bedrock bed, the material on the upper side of the crack (ice) is significantly more compliant than the material on the lower side (rock) and therefore is responsible for most of the crack opening. For this bimaterial case, then, we make the approximation that the actual physical opening displacement $h(x, t)$ is a fraction of the imagined opening $w(x, t)$ in the homogeneous medium of the more compliant material (ice), so that $h(x, t) = \xi w(x, t)$ where $\xi < 1$ (e.g., compare Figures 1 and 2). Thus, in all calculations done here, the physical crack opening h is interpreted to be exactly ξw where w is the opening calculated for the same crack face pressure distribution in a homogeneous ice medium by Equation (7). (Our model could also be applied to englacial cracks, if not too near the bed or surface, by simply removing the factor ξ from all expressions.) In Appendix A of Text S1 we provide justification of this approximation based on elastic analyses of cracks along bimaterial interfaces, and suggest that

$$\xi \approx \frac{1 + E'_{ice}/E'_{bed}}{2} \approx 0.55 \tag{8}$$

is an appropriate factor for ice in contact with (or separating from) bedrock. (We expect that value to be reasonable too for separation from heavily compacted till.) In using Equation (6), then

$$-\frac{\partial}{\Delta p}\partial x = \frac{f_0}{4\xi^{4/3}}\rho U^2 \frac{k^{1/3}}{w^{4/3}} = 0.0793\,\rho U^2 \frac{k^{1/3}}{w^{4/3}}. \quad (9)$$

Finally, if we assume an incompressible fluid (i.e. constant ρ) then the mass conservation equation (setting $h = \xi w$ and canceling the ξ) can be written as

$$\frac{\partial(wU)}{\partial x} + \frac{\partial w}{\partial t} = 0. \quad (10)$$

Note that for steady state cracking with uniform crack-tip velocity U_{tip}, such that $w(x, t) = w(x - U_{tip}t)$, Equation (10) simplifies to $U(x, t) = U_{tip}$ [Desroches et al., 1994], i.e. the thickness-averaged fluid velocity is everywhere equal to the crack-tip velocity. This result will also apply asymptotically, near the tip, for non-steady configurations and time-variable U_{tip}. (Throughout this analysis, we assume the crack to be completely filled with fluid, i.e., with negligible 'fluid lag', a reasonable assumption given the relatively large confining stresses of interest and large (e.g., $\gg$ 10 m) length scales [Garagash and Detournay, 2005].)

2.3. Adaptation of the Power Law Viscous Fluid Crack Solution to the Turbulent Case, Simple Approximate Model

[10] In this section, we follow Desroches et al. [1994] and begin with a steady state solution for a semi-infinite crack, $U(x, t) = U_{tip}$ and so drop the explicit x and t dependence on U. Since there is no explicit time dependence in the other two governing equations, we also drop the explicit t dependence of $w(x, t)$ and $\Delta p(x, t)$ for that semi-infinite case, instead writing $w(x)$ and $\Delta p(x)$. In Section 2.5, we will revert to Equation (10).

[11] At this point, we observe that Equation (9) has the same form as the power law viscous flow lubrication equation [Bird et al., 1987], which can be written as

$$-\frac{d\Delta p}{dx} = \frac{c_0}{w^{1+m}}, \quad (11)$$

where w is the crack opening width, m is the power law index relating shear stress τ with shear rate $\dot{\gamma}$ ($\tau \propto \dot{\gamma}^m$), and c_0 is a factor that includes a dependence on the now uniform U (c_0 is proportional to U^2 for our turbulent case and to U^m for the Desroches et al. [1994] power law case). Thus, by simply using the $m = 1/3$ case, and recalling that U is constant, we can utilize the same procedure as in the work of Desroches et al. [1994], which yields a solution of the same form for both $w(x)$ and $\Delta p(x)$, and obtain (with the crack tip at $x = L$)

$$w(x) = \frac{14A}{3E'} R^{6/7} \tan\frac{\pi}{7}, \quad (12)$$

and

$$\Delta p(x) = P - AR^{-1/7}, \quad (13)$$

where $R \equiv L - x$ is the distance along the crack behind the crack tip, P is a constant which is undetermined in this analysis, and the constant A is directly relatable to $U_{tip} = \dot{L}$ through substitution into Equation (9) (with $U = U_{tip}$). Solving for A gives

$$A = E'\left[\frac{(7/4)^3(3/14)^4 \cdot f_0^3}{\tan^4(\pi/7)\cdot\xi^4}\left(\frac{\rho U_{tip}^2}{E'}\right)^3 \cdot k\right]^{1/7}$$

$$= 0.489E'\left(\frac{\rho U_{tip}^2}{E'}\right)^{3/7} k^{1/7}. \quad (14)$$

Note that A here corresponds to $A'\cos(\pi/7)$ where A' is introduced in Appendix B in Text S1. Stresses within the elastic medium σ_{xx}, σ_{yx} and σ_{yy} can similarly be expressed in polar coordinates (r, θ) around the crack tip, for example, with

$$\sigma_{yy} = -P + r^{-1/7}AF_{yy}(\theta). \quad (15)$$

Full expressions for all stresses, from which F_{yy} may be determined, are given in Appendix B in Text S1. This solution, which is obtained by seeking an appropriate analytic function representation of the Muskhelishvili [1953] potentials or, equivalently, by assuming a Williams [1952] power law stress field near the crack tip, is an exact steady state solution of the governing equations of elasticity and fluid flow for a semi-infinite crack, and it represents the leading-order near crack-tip singularity part of the full solution in other cases. However, it cannot in general satisfy appropriate boundary conditions away from the crack tip or at the glacier surface.

[12] We can, nevertheless, follow Desroches et al. [1994] and use that solution as a basis of an approximate analysis for a finite crack of length $2L$ (see Figure 1). That involves assuming that Equation (13), with $R = L - |x|$, holds over all of $0 \leq |x| \leq L$, and then by choosing P so that the stress intensity factor (K_I) due to $\Delta p(x) \equiv p - \sigma_0$ is zero (otherwise, the asymptotically correct form of the crack opening profile as in Equation (12) would be violated since fracture mechanics requires $K_I = K_{Ic}$ under quasi-static loading, and we are working in a regime for which K_{Ic} is negligible compared to the relevant combination $\Delta p(0)\sqrt{\pi L}$). To accomplish that, we set

$$K_I \equiv \int_0^L \frac{\Delta p(x)dx}{\sqrt{L^2 - x^2}} = K_{Ic} = 0, \quad (16)$$

which gives $P = 1.36934AL^{-1/7}$. Writing this approximation in terms of the inlet excess pressure $\Delta p_{in} \equiv \Delta p(0)$ (instead of as a function of U_{tip}) then yields

$$\Delta p(x) = \Delta p_{in} + 2.7075\Delta p_{in}\left[1 - \left(\frac{L}{L - x}\right)^{1/7}\right]. \quad (17)$$

This approximation is consistent with the neglect of fracture energy (see Figure 2), but ignores the presence of the free surface at the top of the glacier (i.e. it assumes $L \ll H$). Although not completely appropriate, we will use the solution for the entire range of L, including when $L > H$.

[13] With Equation (17) describing the pressure along the crack face, then Equation (12) gives

$$
\begin{aligned}
w(x) &= \frac{2.7075}{\delta} L \frac{\Delta p_{in}}{E'} \left(\frac{L-x}{L}\right)^{6/7} \\
&= 6.0843 L \frac{\Delta p_{in}}{E'} \left(\frac{L-x}{L}\right)^{6/7},
\end{aligned}
\tag{18}
$$

for $0 < x < L$, where

$$
\delta \equiv \frac{3}{14 \tan(\pi/7)} = 0.4450.
\tag{19}
$$

Finally, inserting Equations (17) and (18) into Equation (9) and rearranging gives an expression for U_{tip} in terms of known (or potentially measurable) quantities

$$
\begin{aligned}
U_{tip} &= \frac{2\,\xi^{2/3}\,2.7075^{7/6}}{(7f_0)^{1/2}\,\delta^{2/3}} \sqrt{\frac{\Delta p_{in}}{\rho}} \left(\frac{\Delta p_{in}}{E'}\right)^{2/3} \left(\frac{L}{k}\right)^{1/6} \\
&= 7.36 \sqrt{\frac{\Delta p_{in}}{\rho}} \left(\frac{\Delta p_{in}}{E'}\right)^{2/3} \left(\frac{L}{k}\right)^{1/6}.
\end{aligned}
\tag{20}
$$

It is of interest to note that if we had used the homogeneous-medium version of Equation (9) ($h = w$), the numerical coefficient would change from 7.36 to 11.0 and the remainder of Equation (20) would remain unchanged. (One can also note that the crack-tip asymptotic solution is applicable in the near-tip region of a penny-shaped crack [e.g., *Savitski and Detournay*, 2002] so that Equation (20) may apply approximately in this case as well.)

2.4. Scaling Analysis

[14] The result of Equation (20) can perhaps be more easily understood through a simple scaling analysis. In this scaling analysis, we let $L = L_0 \hat{L}$, $w(x) = w_0 \hat{w}$, $\Delta p(x) = \Delta p_0 \hat{p}$, and $U = U_0 \hat{U}$, where hatted variables are non-dimensional and variables with a subscript zero are characteristic scales for the respective original variables. Inserting these expressions into Equation (7) gives $w_0/L_0 = \Delta p_0/E'$. Similarly, Equation (9) gives $\Delta p_0/L_0 = \rho U_0^2 k^{1/3}/w_0^{4/3}$. Solving for the velocity scale U_0 then yields

$$
U_0 = \sqrt{\frac{\Delta p_0}{\rho}} \left(\frac{\Delta p_0}{E'}\right)^{2/3} \left(\frac{L_0}{k}\right)^{1/6}.
\tag{21}
$$

If no physics other than that of Equations (7), (9) and (10) enters the problem, then the only reasonable pressure scale is the excess inlet pressure, i.e. $\Delta p_0 = \Delta p_{in}$, and if $L \ll H$ then the instantaneous crack half-length L must be the relevant scale for L_0. That is, given a pressure scale Δp_{in} and a single length scale L, the scaling of Equation (20) is completely determined by dimensional analysis, and only the numerical factor is dependent on the choices made in Section 2.3. One may note, however, that if the crack has an additional length scale (e.g., if $H \sim L$) then both Equation (20) and Equation (21) can have an added dependence on a function of L/H.

2.5. Self-Similar Analysis

[15] Finally, following an approach similar to those of *Spence and Sharp* [1985] and *Adachi and Detournay* [2002], we numerically find an exact self-similar solution, also for the case in which $L \ll H$. After scaling the equations as in Section 2.4, we look for a non-dimensionalized self-similar solution of the form

$$
L(t) = L_0 \hat{t}^\alpha / \alpha,
\tag{22a}
$$

$$
w(x,t) = w_0 \hat{t}^\beta \hat{w}(\hat{x}) / \beta,
\tag{22b}
$$

$$
\Delta p(x,t) = \Delta p_0 \hat{p}(\hat{x}),
\tag{22c}
$$

$$
U(x,t) = \phi U_0 \hat{t}^\gamma \hat{U}(\hat{x}).
\tag{22d}
$$

Here, $\hat{t} \equiv \phi U_0 t/L_0$ is a non-dimensional time, $\hat{x} \equiv x/L(t)$ is a non-dimensional position, and α, β, γ and ϕ are numerical constants. It should be observed that L_0 can be chosen arbitrarily (in that it will be seen to cancel from all final expressions). Once L_0 is chosen and the correspondence $\Delta p_0 = \Delta p_{in}$ is made, then w_0 and U_0 are determined by these choices, but $U(x, t)$ has an extra condition to satisfy, $U(L(t), t) = dL(t)/dt$, which is met by proper choice of ϕ. In this self-similar solution, it is assumed that $\Delta p_{in} \equiv \Delta p(0, t)$ is constant so that Equation (22c) does not have any explicit time dependence. Substituting these expressions into Equations (7), (9) and (10), we find that the time dependence can only be satisfied with $\alpha = 6/5$, $\beta = 6/5$, $\gamma = 1/5$ (but ϕ is still to be determined). We therefore find that in this self-similar solution $L(t)$ and $w(x, t)$ grow slightly faster than linearly with time. We are also left with 3 non-dimensional ordinary differential/integral equations for the self-similar displacement profile $\hat{w}(\hat{x})$, pressure profile $\hat{p}(\hat{x})$ and velocity profile $\hat{U}(\hat{x})$. These 3 expressions are

$$
\hat{p}(\hat{x}) = \frac{1}{4\pi} \int_{-1}^{1} \frac{d\hat{w}(\hat{s})}{d\hat{s}} \frac{d\hat{s}}{\hat{x} - \hat{s}},
\tag{23}
$$

$$
-\hat{w}^{10/3} \frac{d\hat{p}}{d\hat{x}} = \frac{(6/5)^{1/3} f_0}{4\xi^{4/3}} \phi^2 \left(\hat{U}\hat{w}\right)^2,
\tag{24}
$$

and

$$
\frac{d\left(\hat{U}\hat{w}\right)}{d\hat{x}} = \frac{d(\hat{x}\hat{w})}{d\hat{x}} - 2\hat{w}.
\tag{25}
$$

Similarly translating boundary conditions gives $\hat{w}(1) = 0$, $\hat{p}(0) = 1$, and $\hat{U}(1) = 1$. Integrating Equation (25) from $\hat{x}$ to 1 and substituting into Equation (24) yields

$$
-\hat{w}^{10/3} \frac{d\hat{p}}{d\hat{x}} = \frac{(6/5)^{1/3} f_0}{4\xi^{4/3}} \phi^2 \left(\hat{x}\hat{w} + 2 \int_{\hat{x}}^{1} \hat{w}(\hat{s})\, d\hat{s}\right)^2.
\tag{26}
$$

[16] It now only remains to numerically solve Equations (23) and (26) subject to $\hat{w}(1) = 0$ and $\hat{p}(0) = 1$. To accomplish this, we follow an approach like that of *Adachi and*
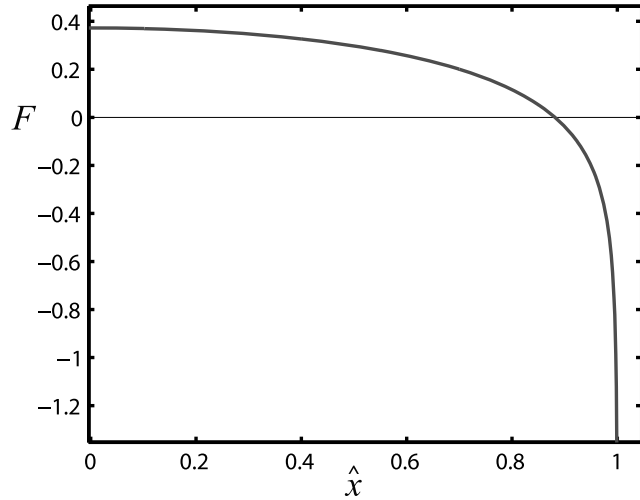
Figure 3. $F(\hat{x})$ as calculated numerically from Equation (30). $F(\hat{x})$ represents the leading-order pressure term in Equation (28).

Detournay [2002] and take the $\hat{w}$ and $\hat{p}$ profiles to be given as series, the first term of which exactly embeds the crack-tip asymptotic (e.g., is consistent with Equations (12–13)) and the rest of the terms which do not contribute a further singularity at the crack tip. That is, we take

$$\hat{w} = D\left[\frac{1}{\delta}\left(\frac{1-\hat{x}^2}{2}\right)^{6/7} + A_1 w_1(\hat{x})\right.$$
$$\left. + A_2 w_2(\hat{x}) + A_3 w_3(\hat{x}) + \ldots\right] \tag{27}$$

and

$$\hat{p} = D\left[F(\hat{x}) + A_1(c_1 - |\hat{x}|).\right.$$
$$\left. + A_2\left(c_2 - \hat{x}^2\right) + A_3\left(c_3 - |\hat{x}|^3\right) + \ldots\right]. \tag{28}$$

Here, c_k are constants chosen to remove any contribution to the stress intensity factor (i.e. consistent with negligible fracture resistance) from each of the $c_k - |\hat{x}|^k$ terms, and thus satisfy

$$K_I = \int_0^1 \frac{\left(c_k - |\hat{x}|^k\right)d\hat{x}}{\sqrt{1-\hat{x}^2}} = 0, \tag{29a}$$

or

$$c_k = \frac{2}{\pi}\int_0^{\pi/2} \sin^k \varphi \, d\varphi, \tag{29b}$$

where the substitution $\hat{x} = \sin \varphi$ was made. $F(\hat{x})$ and the w_k are chosen so that each term of the $\hat{w}$ and $\hat{p}$ expressions pairwise satisfy Equation (23), i.e.,

$$F(\hat{x}) = \frac{1}{4\pi}\int_{-1}^{1} \frac{1}{\delta}\frac{d}{d\hat{s}}\left(\frac{1-\hat{s}^2}{2}\right)^{6/7}\frac{d\hat{s}}{\hat{x}-\hat{s}}$$
$$= -\frac{3}{7 \cdot 2^{6/7}\pi\delta}\int_{-\pi/2}^{\pi/2} \frac{\sin \varphi \cos^{5/7} \varphi \, d\varphi}{\hat{x}-\sin \varphi} \tag{30}$$
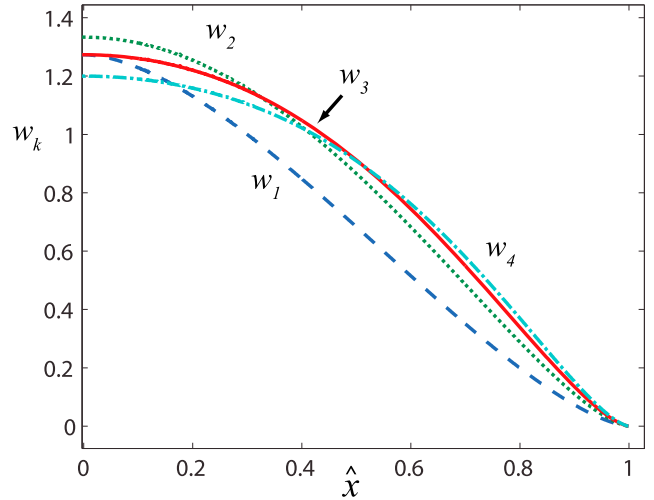
Figure 4. Here $w_k(\hat{x})$ as calculated numerically from Equation (32). The blue dashed line is w_1, the dotted green line is w_2, the solid red line is w_3 and the dashed-dotted cyan line is w_4. The w_k are terms of the displacement opening series (Equation (27)).

and

$$c_k - |\hat{x}|^k = \frac{1}{4\pi}\int_{-1}^{1} \frac{dw_k(\hat{s})}{d\hat{s}}\frac{d\hat{s}}{\hat{x}-\hat{s}}, \tag{31}$$

where Equation (31) can be inverted to solve for w_k using the *Muskhelishvili* [1953] approach. (Pressure and displacement are Hilbert transform pairs and the mixed boundary condition problem is solved with this approach.) This results in non-singular $dw_k/d\hat{x}$ at $|\hat{x}| = 1$, consistent with choosing $w_k(\pm 1) = 0$, provided that the c_k are chosen according to Equation (29b). The result, as simplified by an expression from *Adachi and Detournay* [2002], is (setting $\hat{x} = \sin \varphi$)

$$w_k(\sin \varphi) = \frac{4}{\pi}\int_0^{\pi/2} \left(c_k - \sin^k \theta\right) \ln\left|\frac{\cos \varphi + \cos \theta}{\cos \varphi - \cos \theta}\right| \cos \theta \, d\theta. \tag{32}$$

[17] $F(\hat{x})$ and the $w_k(\hat{x})$ are plotted in Figures 3 and 4, respectively. Values of $w_k(0)$ and averages of $w_k(\hat{x})$ over the crack are tabulated in Table 1.

[18] D and the A_k are then constants to be determined so that the remaining Equation (26) is satisfied. Note that δ is inserted in Equation (27) so that $F(\hat{x}) \cdot [(1-\hat{x}^2)/2]^{1/7} \to -1$ as $\hat{x} \to \pm 1$. Equation (26) can be satisfied by choosing ϕ and the A_k coefficients appropriately, and the boundary condition $\hat{p}(0) = 1$ can be satisfied by choosing D appropriately.

Table 1. Values of $w_k(0)$ and Average Value of $w_k(\hat{x})$ up to $k = 4$[a]

	w_1	w_2	w_3	w_4
Value at $\hat{x} = 0$	$4/\pi$	$4/3$	$4/\pi$	$6/5$
Average value	$2/3$	$\pi/4$	$4/5$	$\pi/4$

[a]Average values are numerically calculated but agree with stated exact result to within numerical error.
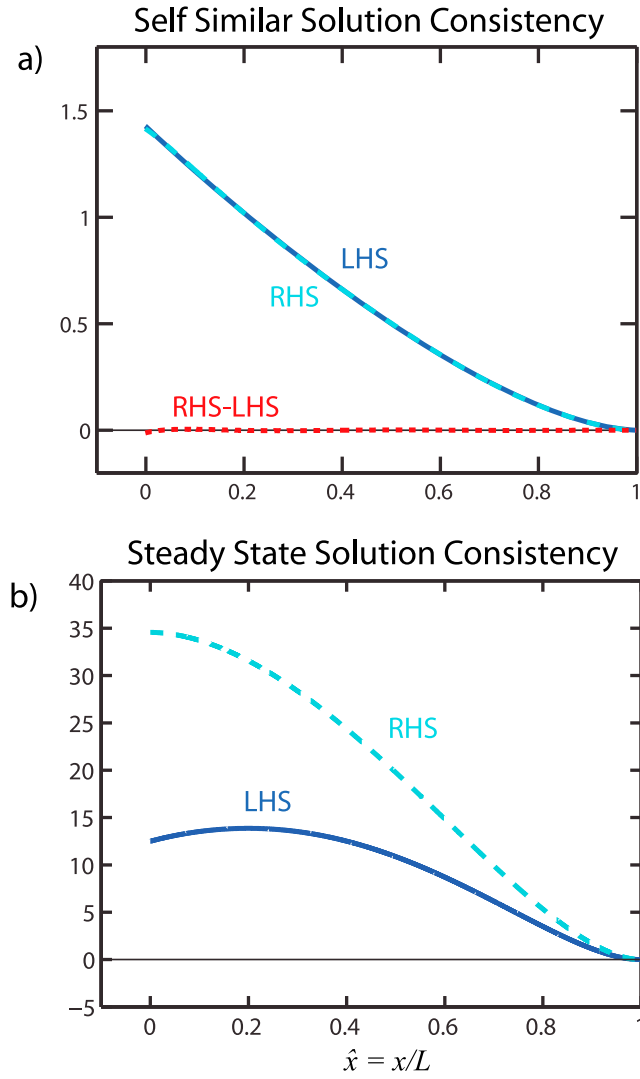
a)

b)

Figure 5. (a) Plotted are the *LHS* (solid blue) and *RHS* (dashed cyan) of Equation (26) and the difference *RHS* − *LHS* (dotted red) for the self-similar solution. (b) For comparison with Figure 5a, plotted are the analogous *LHS* and *RHS* of a scaled version of Equation (9) multiplied by $w^{10/3}$ on both sides, using w as calculated to be consistent with the steady state Δp in Equation (7). These comparisons quantify how well the solutions perform. As expected, the steady state solution is consistent asymptotically as $\hat{x} \to 1$ but, unlike the self-similar solution, has significant differences away from $\hat{x} = 1$.

To determine ϕ, we substitute Equations (27)–(28) into Equation (26) and take the limit as $\hat{x} \to 1$. The resulting limit is independent of the A_k and gives

$$(6/5)^{1/6}\phi = \frac{2\xi^{2/3}D^{7/6}}{(7f_0)^{1/2} \cdot \delta^{2/3}}. \tag{33}$$

Note that $(6/5)^{1/6}\phi$ is the numerical coefficient in Equation (22d) analogous to the 7.36 coefficient of Equation (20), and unsurprisingly has the same functional dependence on f_0, ξ, and δ. To determine the A_k, we minimize the normalized

squared error between the left-hand-side (*LHS*) and right-hand-size (*RHS*) of Equation (26). That is, we minimize

$$\epsilon_m \equiv \frac{\sum_i [RHS(\hat{x}_i) - LHS(\hat{x}_i)]^2}{\left[\sum_i LHS(\hat{x}_i)\right]^2} \tag{34}$$

over equally spaced points $\hat{x}_i$ between 0 and 1. (This solution technique is a standard collocation method using equally spaced collocation points.) We find that using only 5 terms in the series (including up to the A_4 term) gives an adequate minimization of ϵ_m, as shown in Figure 5a. (See also Figure 5b for the analogous comparison for the steady state solution.) As in the work of *Spence and Sharp* [1985], the resulting values of A_k are relatively insensitive to the exact choice of misfit functional ϵ_m. The values obtained for D, A_k and c_k are given in Table 2, and the resulting profiles for $\hat{w}$ and $\hat{p}$ are shown in Figure 6 compared to the profiles for the approximate solution of Section 2.3. The $\hat{U}$ profile is shown in Figure 7. This value of D results in

$$(6/5)^{1/6}\phi = 5.17, \tag{35}$$

a 30% reduction from the 7.36 coefficient of Equation (20).

[19] One can explicitly find $L(t)$ by solving Equation (22a) in terms of all the now known quantities to obtain

$$L(t) = \frac{5\phi^{6/5}U_0^{6/5}}{6L_0^{1/5}}t^{6/5}$$
$$= \frac{5}{6}\phi^{6/5}\left(\frac{\Delta p_{in}}{\rho}\right)^{3/5}\left(\frac{\Delta p_{in}}{E'}\right)^{4/5}\frac{t^{6/5}}{k^{1/5}}, \tag{36}$$

so that

$$U_{tip} \equiv \frac{dL}{dt} = U(L(t),t) = (6/5)^{1/6}\phi U_0\left(\frac{L(t)}{L_0}\right)^{1/6}$$
$$= (6/5)^{1/6}\phi\sqrt{\frac{\Delta p_{in}}{\rho}}\left(\frac{\Delta p_{in}}{E'}\right)^{2/3}\left(\frac{L(t)}{k}\right)^{1/6}, \tag{37}$$

and

$$w(x,t) = L(t)\frac{\Delta p_{in}}{E'}\hat{w}(\hat{x})$$
$$= \frac{2.002}{\delta}L(t)\frac{\Delta p_{in}}{E'}\left[\left(\frac{L(t)^2 - x^2}{2L(t)^2}\right)^{6/7} + \delta A_1 w_1(\hat{x})\right.$$
$$\left. + \delta A_2 w_2(\hat{x}) + \delta A_3 w_3(\hat{x}) + \cdots\right]. \tag{38}$$

Table 2. Self-Similar Parameters D, A_k, and c_k

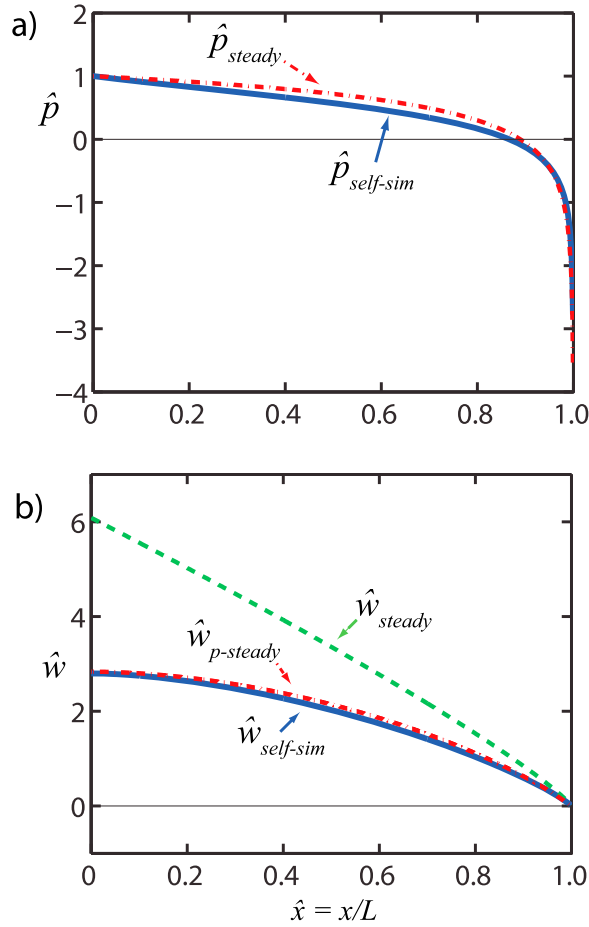| Parameter	Value
D	2.002
A_1	0.463
A_2	−0.522
A_3	0.407
A_4	−.0212
c_1	$\frac{2}{\pi}$
c_2	$\frac{1}{2}$
c_3	$\frac{4}{3\pi}$
c_4	$\frac{3}{8}$

Figure 6. Comparison of steady state and self-similar solutions. (a) Plotted are the $\hat{p}$ (scaled pressure) for the self-similar solution ($\hat{p}_{self\text{-}sim}$) and the steady state solution ($\hat{p}_{steady}$). The actual pressure is given by $p(x) = \Delta p_{in}\hat{p}(\hat{x})$. (b) Plotted are the $\hat{w}$ (scaled model opening) for the self-similar solution ($\hat{w}_{self\text{-}sim}$), the $\hat{w}$ of Equation (18) for the steady state solution ($\hat{w}_{steady}$), and the $\hat{w}$ consistent with the steady state $\hat{p}_{steady}$ distribution in Equation (7) ($\hat{w}_{p\text{-}steady}$). The actual opening is given by $h(x) = \xi w(x) = \xi L(t)\Delta p_{in}/E' \cdot \hat{w}(\hat{x})$.

[20] For later reference, $\hat{w}(0) = 2.799$ and the average value of $\hat{w}$ is 1.849 so that the maximum actual crack opening is given by $h(0) = 1.539L(t)\Delta p_{in}/E'$ and the average value of h is given by

$$h_{avg} = 1.017L(t)\,\Delta p_{in}/E'. \tag{39}$$

3. Understanding Glacial Crack Propagation

[21] The basic problem which we have solved is a critical component of understanding glacial under-flooding but is still far from sufficient to fully interpret (or rationalize) observations. In the section that follows, we outline a scheme for utilizing the results of Section 2 to understand one set of observations. A number of unrealistic assumptions are found to be necessary in this first attempt to treat the observed scenario, and a quantitatively precise treatment

with realistic assumptions will likely only be possible after an extensive research program is conducted, which is well beyond the scope of this paper. Nevertheless, we show some preliminary results that are meant to give the reader an idea for how future results can be compared with observations.

[22] To apply the results of the previous section to crack propagation at the bed of a glacier, we must estimate the parameters that enter Equation (37). Here, to make direct contact with the observations of *Das et al.* [2008] of GPS displacements associated with the drainage of a Greenland meltwater lake, we take the margin of the Greenland Ice Sheet as the region of interest. Key observations of theirs, which we later compare our model results with, include an average drainage rate of $8.7 \cdot 10^3$ m^3/s during the ≈ 2 hour event, ≈ 1.1 m vertical displacements, ≈ 0.8 m northward displacements, and an increased westward velocity (by a factor of 3 for the daily average). Estimates of the Young's modulus of glacial ice varies substantially, with a range of 0.9–10 GPa [*Vaughan*, 1995]. We choose, as representative, laboratory values of Young's modulus at $-5°C$ of $E = 6.2$ GPa [*Jellinek and Brill*, 1956] and Poisson's ratio $\nu = 0.3$ [*Vaughan*, 1995], giving $E' = 6.8$ GPa. This value may be appropriate if the displacements have a linear elastic response, but may be an overestimate if there is a significant visco-elastic response. Fluid density is taken as $\rho = 1000$ kg/m^3 and ice density is taken as $\rho_{ice} = 910$ kg/m^3. The study area of *Das et al.* [2008] had 980 m-thick ice ($H = 0.98$ km), so the pressure at the base of the ice sheet in excess of the ice pressure due to a column of standing water there would be $\Delta p_{static} = (\rho - \rho_{ice})gH_w \approx 0.87$ MPa, where the height of water, H_w, is taken as equal to the ice thickness, H, and $g \approx 9.81$ m/s^2. The actual excess pressure at the inlet is reduced from this value due to frictional losses from the surface to the bed, but as a high-end first approximation we take $\Delta p_{in} = \Delta p_{static} = 0.87$ MPa. The channel roughness k is the least constrained of all parameters but is likely a healthy but
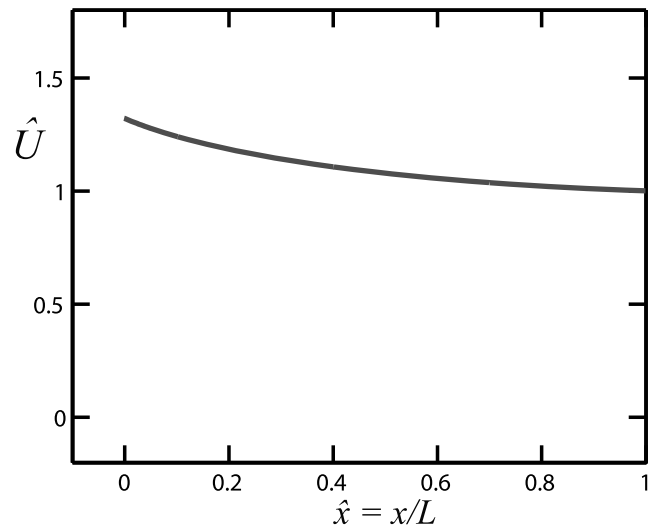

Figure 7. Plotted is the $\hat{U}$ (scaled fluid velocity) for the self-similar solution. $\hat{U}(0) \approx 1.321$, and $\hat{U}(1) = 1$ as required by the condition $U(L) = U_{tip}$. For comparison, the steady state solution has $\hat{U}(\hat{x}) \equiv 1$. The actual fluid velocity is given by $U(x) = (6/5)^{1/6}\phi U_0(L(t)/L_0)^{1/6}\hat{U}(\hat{x})$.

small fraction of the channel opening (with range perhaps being 0.005 m < k < 0.2 m). Luckily the dependence of U_{tip} on k is quite weak (power law with an exponent of one sixth) so we take a reasonable estimate of $k \approx 1$ cm, which is consistent with a Manning roughness of $n \approx 0.018$ s m$^{-1/3}$ (a lower value than is used by many authors for subglacial channels [*Roberts*, 2005; *Hooke*, 2005]). Taking $L = H \approx$ 1.0 km and substituting these values into Equation (37) then yields a (maximum) estimate of $U_{tip} = 2.6$ m/s and average opening $h_{avg} = 13$ cm. The dependence on L is also weak so that with $L = 0.2$ km, we would have $U_{tip} = 2.0$ m/s, although h_{avg} scales in proportion to L so that $h_{avg} = 2.6$ cm. The volume accommodated is $2Lh_{avg}L_c = 2L^2 L_c(h_{avg}/L)$, where L_c is an effective length perpendicular to the plane of straining for which the solution is approximately valid. This gives a volumetric flow rate of $4L_c h_{avg}U_{tip}$. Taking $L_c \approx$ 3 km (approximately the length of the observed surface breaking by *Das et al.* [2008]) then for $L = 1.0$ km, we can estimate a flow rate of about $4.1 \cdot 10^3$ m^3/s (as compared with the average flow rate of $8.7 \cdot 10^3$ m^3/s observed by *Das et al.* [2008]).

[23] As discussed earlier, our analysis assumes high Reynolds number, ignores any channelized or sloping bed topography, neglects fracture energy and assumes a lubrication approximation with neglect of the acceleration term of the full Navier-Stokes equation. We verify that these approximations are reasonable for the Greenland basal crack situation considered here. Taking $U \gtrsim 2$ m/s, $h \gtrsim 0.1$ m (which apply for crack lengths of interest $L \gtrsim 1$ km), $\rho \approx$ 10^3 kg/m^3, and viscosity of $\mu \approx 1.8 \cdot 10^{-3}$ Pa s, then $\Re \gtrsim 10^5$, which puts it in the fully turbulent regime. The hydraulic head gradient is given by $S \approx \Delta p_{in}/(\rho g L) \approx 0.1$ so that bed slopes $\ll 5°$ can be safely ignored. Taking ice fracture toughness of $K_{Ic} \approx 0.16$ MPa m$^{1/2}$ [*Rist et al.*, 1999], which is slightly on the high side of estimates by *Ashby* [1989] and *Fischer et al.* [1995], and surely higher than for the ice-rock interface (regardless of whether the ice is frozen to the bedrock or not), we can compare the total energy lost in the pressure gradient (per unit surface area of the crack), $e_{loss} \equiv$ $E_{loss}/Area \approx \Delta p_{in}h \gtrsim 0.9 \cdot 10^5$ J/m^2, with the fracture energy $K_{Ic}^2/E \approx 4.1$ J/m^2. Since the pressure gradient energy loss is much greater than the fracture energy (except at the very earliest stages of crack growth, when $h \lesssim 10^{-5}$ m or equivalently $L \lesssim 0.1$ m), it is reasonable to neglect the fracture energy. This inequality is analogous to the one suggested by *Savitski and Detournay* [2002] and *Bunger and Detournay* [2008] for Newtonian viscous flows; unlike in their analysis, which is for constant inflow rate, our constant Δp_{in} solution has negligible fracture energy during the later stages of crack growth (and is only toughness dominated at the very earliest stages). Another appropriate view is to consider the ratio $K_{Ic}/(\Delta p_{in}\sqrt{\pi L})$, where the denominator is a nominal K_I that would result from uniform pressurization. This ratio is ≈ 0.1 when $L = 1$ m, and is $\lesssim 0.01$ for $L > 100$ m. We further note that the small crack-tip velocity (<10 m/s) compared to elastic wave speeds (>100 m/s) implies that elastodynamic effects are unimportant, validating our use of $K_I = K_{Ic}$. Finally, $\rho U^2 \lesssim 10^4$ Pa as compared with $\Delta p_{in} \approx 8 \cdot 10^5$ Pa so that the acceleration term of the Navier-Stokes equation $\rho(\partial U/\partial t + U \partial U/\partial x)$, of order $\rho U^2/L$, can be neglected compared with the pressure gradient term ($\partial p/\partial x$), of order $\Delta p_{in}/L$.

3.1. Approximations for Comparison With Observations

[24] As suggested above, one potential application of our turbulent hydraulic fracture model is to rapid drainage from supraglacial meltwater lakes to the bed of an ice sheet. For this application, it is useful to compare our model results with the observations of *Das et al.* [2008], in which they were able to measure the supraglacial lake water level as well as vertical and horizontal surface displacements during the rapid drainage event. A rough comparison of modeled and observed flow rates was given above for a plausible choice of parameters, but in order to quantitatively compare our model results with these observations, there are a number of issues that must be dealt with. We stress the fact that these issues are not all solved satisfactorily, but a number of crude approximations are suggested. The following 5 topics will be addressed.

[25] First, in Section 3.1.1, we make estimates to calculate the net volumetric flow rate into the basal crack and the total water volume taken up by the crack system. As part of this calculation, we observe that it is necessary to also consider the flow rate and volume contributions from the vertical crack that connects the surface to the basal crack.

[26] Second, in Section 3.1.2, we estimate the vertical and horizontal surface displacements.

[27] For both of these calculations, we observe that the 3D nature of the true situation is important, whereas our calculations of Section 2 are all done in (2D) plane strain. Thus, in Section 3.1.3, we propose an ad-hoc procedure for interpreting our plane strain results for a circular crack.

[28] In Section 3.1.4, we find that an additional deficiency of our model is the unrealistic approximation $L \ll H$ and we discuss two possible approaches of utilizing our results nonetheless.

[29] The last issue we discuss here (in Section 3.1.5) is the fact that the excess pressure at the basal crack inlet (Δp_{in}) is not known a priori because of the pressure loss on the way from the surface to the bed, and hence it must be determined in conjunction with the rest of the calculation.

[30] Finally, in Section 3.1.6, we summarize the resulting 3 model choices that arise from using the approximations discussed throughout this section. It should be noted, however, that some of the difficulties discussed are substantial and overcoming all of them is beyond the scope of this paper. We therefore reiterate that the following sections allow only for crude estimates of the desired quantities, and the results of this paper beyond Section 2 should only be taken as rough preliminary estimates.

3.1.1. Calculation of Flow Rates and Volumes

[31] We first discuss how to calculate volumes and flow rates within our turbulent self-similar solution, which strictly applies only in the range $L \ll H$. In order to later allow these results to be generalized from 2D plane strain to a 3D geometry in Section 3.1.3, and later to arbitrary L/H in Section 3.1.4), we find it useful to compare our self-similar solution to the (static) solution for a crack opened by a uniform pressure, taken to be Δp_{in}, over the entire crack
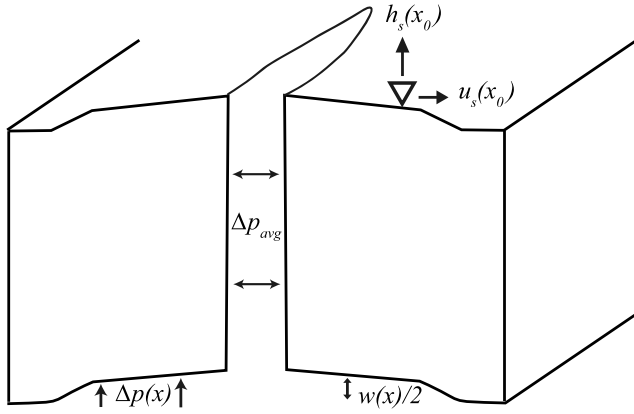
Figure 8. Schematic of surface displacements at a distance x_0 from the center of the connecting conduit. As discussed in the text, the vertical displacement is calculated using Equation (50), and the horizontal displacement is approximated with Equation (51) as being due to an average pressure Δp_{avg} along the connecting conduit face.

face. For this uniform pressure plane strain crack of (instantaneous) length $2L$ in a homogeneous medium, the crack opening profile is given by

$$w_U(x) = \frac{4\Delta p_{in}L}{E'}\sqrt{1 - \hat{x}^2}, \qquad (40)$$

where, as before, $\hat{x} \equiv x/L$ [see, e.g., *Tada et al.*, 2000]. Approximately accounting for the bimaterial case, as before, the average opening is then given (as a function of L) by

$$\overline{h}_U = \xi\overline{w}_U = \frac{\xi}{2L}\int_{-L}^{L} w_U(x)dx = \frac{\xi\pi\Delta p_{in}L}{E'}. \qquad (41)$$

[32] Now, we show that both the volume and flow rate can be expressed in terms of $\overline{h}_U$ and $L(t)$ (which is known from the self-similar solution, Equation (36)). Comparing the self-similar openings of Equations (38) and (39) with the uniform pressure openings of Equation (40) and (41), we observe that we can write

$$h(x) = \frac{\overline{h}_U}{\pi}\hat{w}(\hat{x}), \qquad (42)$$

and

$$h_{avg} = C_1\overline{h}_U \qquad (43)$$

where C_1 is given by $C_1 = 1.859/\pi = 0.592$. We can then express the 2D crack volume V_{2D} (i.e., area of crack opening in the x-y plane) as

$$V_{2D}(t) = 2h_{avg}(t) \cdot L(t) = 2C_1\overline{h}_U(t)L(t), \qquad (44)$$

where $\overline{h}_U$ is given as a function of L in Equation (41). Similarly, the 2D flow rate Q_{2D} is given by

$$Q_{2D} = \frac{dV_{2D}}{dt} = 2C_1\frac{d(\overline{h}_U L)}{dL} \cdot \frac{dL}{dt} = 2C_1\frac{d(\overline{h}_U L)}{dL} \cdot U_{tip}. \qquad (45)$$

Without modification, the $\overline{h}_U$ of Equation (41) substituted into Equation (45) gives $d(\overline{h}_U L)/dL = 2\,\overline{h}_U$ and thus $Q_{2D} = 4\overline{h}_U U_{tip}$. Furthermore, the self-similar solution for U_{tip} (Equation (37)) can be rewritten in terms of $\overline{h}_U$ by substituting $\Delta p_{in}/E' = \overline{h}_U/(\xi\pi L)$ such that

$$U_{tip} = C_2\sqrt{\frac{\Delta p_{in}}{\rho}}\left(\frac{\overline{h}_U}{L}\right)^{2/3}\left(\frac{L}{k}\right)^{1/6}, \qquad (46)$$

with

$$C_2 = \frac{(6/5)^{1/6}\phi}{(\xi\pi)^{2/3}} = \frac{2D^{7/6}}{(7f_0)^{1/2}(\pi\delta)^{2/3}} \approx 3.571. \qquad (47)$$

Thus, for a given L, we can calculate $\overline{h}_U$ through Equation (41), and then calculate V_{2D} through Equation (44) and Q_{2D} through Equation (45).

[33] We note that the vertical crack (moulin) system connecting the surface to the basal crack likely contributes to both the volume of water stored as well as surface displacements. To estimate these quantities for the vertical connecting crack, we approximate this additional crack as being a plane stress center crack of length $2a$ in a homogeneous body, opened by a uniform pressure equal to the depth-averaged pressure in excess of hydrostatic ice pressure (see Figure 8). This approximation is only valid if stresses in the solid (ice) are close to hydrostatic and is not accurate if the region has high extensional or compressional horizontal stresses. Furthermore, this plane stress crack will only be opened significantly if basal shear stresses are low, suggesting that $a < L$ (where we anticipate the 3D geometry of the basal crack as being close to circular, as will be suggested below). Finally, the depth-averaged treatment of the vertical crack is clearly a crude approximation to the true situation in which excess pressure and opening varies with depth, but may be a reasonable first approximation. With these caveats, this elliptically shaped connecting crack then has volume given by

$$V_c = \pi a u_0 H_w = \frac{2\pi\Delta p_{avg}a^2 H_w}{E} \qquad (48)$$

where $2u_0$ is the crack center opening, and $\Delta p_{avg} \approx \Delta p_{in}/2$ is taken as the depth-averaged pressure in excess of the local hydrostatic pressure. Contribution to flow rate is calculated, as above, to be

$$Q_c = \frac{dV_c}{dt} = \frac{dV_c}{da} \cdot \frac{da}{dt} = \frac{4\pi\Delta p_{avg}aH_w}{E} \cdot \frac{da}{dt}. \qquad (49)$$

3.1.2. Surface Displacements

[34] Here, we calculate model vertical and horizontal surface displacements based on the basal plane strain self-similar crack solution and the approximate plane stress connecting crack. As shown in Appendix C in Text S1, vertical surface displacements can be calculated using the reciprocal theorem and Boussinesq-Flamant line source solution [see, e.g., *Timoshenko and Goodier*, 1987]. It is also shown that the horizontal opening of the vertical crack has a negligible contribution to the vertical surface displacements compared with the contribution from the basal

crack opening. In Appendix C in Text S1, we also show that the horizontal surface displacements can be approximated by calculating the horizontal opening of the (vertical) connecting crack in a plane stress configuration. These calculations result in the following expressions for vertical (h_s) and horizontal (u_s) displacements at a surface location x_0 (relative to the crack inlet at $x = 0$ and in the plane of crack growth, see Figure 8). The vertical displacement is

$$h_s(x_0) \approx \frac{H^3 \overline{h}_U}{\xi \pi^2 L^3} \int_{-1}^{1} \frac{\hat{w}(\hat{x}) \, d\hat{x}}{\left[(\hat{x} - \hat{x}_0)^2 + \hat{H}^2 \right]^2}, \tag{50}$$

where $\hat{H} \equiv H/L(t)$, $\hat{x}_0 = x_0/L(t)$, $\hat{w}(\hat{x})$ is the scaled self-similar opening given in Equation (27), and other variables are as before. The horizontal displacement is

$$u_s(x_0) = \frac{2\Delta p_{avg} a}{E} \left[\sqrt{1 + (x_0/a)^2} - (x_0/a) \right. \\ \left. + \frac{1+\nu}{2} (x_0/a) \left(1 - \frac{x_0/a}{\sqrt{1 + (x_0/a)^2}} \right) \right], \tag{51}$$

where Δp_{avg} is the constant average pressure assumed along the crack face. Thus, given a surface location x_0 and crack length $L(t)$, Equation (50) gives h_s in terms of our self-similar solution and Equation (51) gives u_s in terms of Δp_{avg}.

3.1.3. Generalization From Plane Strain to 3-D

[35] Since the previous expressions are for an unrealistic 2D plane strain geometry (for example, true volume is not easily defined for the basal crack), it is useful to generalize this to a 3D geometry. We do this in the following, somewhat ad-hoc manner. First, we note that the 3D crack opening can be expected to be close to circular since a shorter crack length in a particular direction would be more unstable to growth under the same loading conditions. Thus, for this 3D extension, we first consider a (circular) penny-shaped crack of radius L in a homogeneous medium, loaded with uniform pressure Δp_{in} and clamped on the edges. For this uniform loading case, *Sneddon* [1946] gives

$$w_U^{3D}(\mathcal{R}) = \frac{8\Delta p_{in} L}{\pi E'} \sqrt{1 - \hat{\mathcal{R}}^2}, \tag{52}$$

where $\hat{\mathcal{R}} \equiv \mathcal{R}/L$ and $\mathcal{R}$ is distance from the center of the crack. Approximately accounting for the bimaterial case, as before, the average opening is then

$$\overline{h}_U^{3D} = \xi \overline{w}_U^{3D} = \frac{\xi}{\pi L^2} \int_0^L 2\pi \mathcal{R} w_U^{3D}(\mathcal{R}) d\mathcal{R} = \frac{16\xi \Delta p_{in} L}{3\pi E'}. \tag{53}$$

Comparing the penny-shaped openings of Equation (52) and Equation (53) with the 2D plane-strain openings of Equation (40) with Equation (41), we observe that the two constant pressure loading cases have opening displacements with identical functional forms and have average openings that differ by a factor of $16/(3\pi^2) \approx 0.540$. With this in mind, we use the following plausible ad-hoc procedure that approximately accounts for the 3D penny-shaped geometry in the turbulent flow case. We utilize the same plane strain

displacement profile $\hat{w}(\hat{x})$ on the penny-shaped crack $\hat{w}(\hat{r}) = \hat{w}(\hat{x})$ as well as utilize the same scaling factors C_1 and C_2, but replace all instances of $\overline{h}_U$ by $\overline{h}_U^{3D}$ (i.e. in Equations (42), (43), (46), and (50)). In this way, we can now calculate a true basal crack volume,

$$V_b = C_1 \pi L^2 \overline{h}_U^{3D}, \tag{54}$$

a corresponding flow rate,

$$Q_b = \frac{dV_b}{dt} = \frac{dV_b}{dL} U_{tip}, \tag{55}$$

and appropriately scale the vertical displacement (Equation (50)) to account for the added stiffness of the 3D geometry. (We note that for this circular crack geometry, the 2D solution of Equation (50) is an upper bound to the true uplift and is only a good approximation when $x_0 \lesssim L$.) The horizontal displacement of Equation (51) is unaffected by this procedure. We note that future work is necessary to check the validity of this scaling procedure since, for example, the constants C_1 and C_2 for a penny-shaped crack could easily be different than those chosen based on the 2D plane-strain solution. We also note that (3D) volumes can be estimated for the plane strain solution by replacing the $\overline{h}_U^{3D}$ of Equation (54) with $\overline{h}_U$.

3.1.4. Using the Model Beyond $L \ll H$

[36] As previously mentioned, the results presented are strictly only applicable when $L \ll H$. In Appendix D in Text S1 we estimate that L becomes as large as $L \gtrsim 5.25$ km (as compared with $H \approx 1$ km), well beyond the appropriate range of usage of the approximation $L \ll H$.

[37] Fully addressing this issue requires treating the free surface boundary condition properly and is beyond the scope of this paper. However, preliminary calculations that include the free surface suggest that order-of-magnitude bounds on the final results can be estimated using two simple scalings. We emphasize that the two approaches used here should not be expected to give better than order-of-magnitude accuracy, and future work is necessary to determine the degree of accuracy.

[38] In the first approach, we simply apply our previous model results in all regimes of L/H, despite L growing significantly larger than H. The weak dependence of Equation (37) on L lends some credibility to using the $L \ll H$ solution beyond its known range of usability, although preliminary calculations suggest substantial inaccuracies. In a second approach, we attempt to approximately account for the range beyond $L \ll H$ by matching our solution with a plate theory (beam theory) scaling applicable in the limit $L \gg H$. For this latter approach, we again find it convenient to compare with the constant loading case and, as shown in Appendix D in Text S1, obtain an average opening given by

$$\overline{h}_U^S = \frac{16\xi \Delta p_{in} L}{3\pi E'} \left[1 + \frac{3\pi}{256\xi} \cdot \frac{L^3}{H^3} \right]. \tag{56}$$

This approximation asymptotically satisfies both solutions in the appropriate limits and defines a smooth transition between them. The validity of this 'linear sum' transition is unknown and unfortunately untestable within the scope of the current work, but we hope to address the validity of this approximation in future work. If the transition is strongly
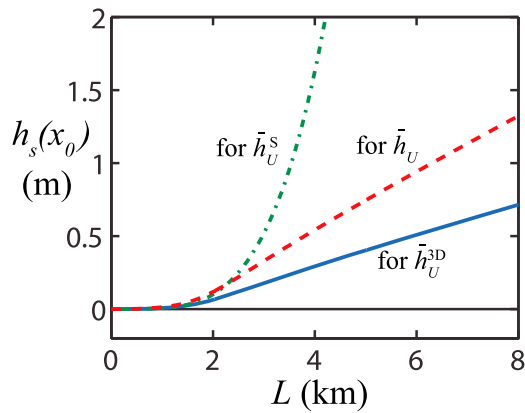
Figure 9. Surface displacements at $x_0 = 1.7$ km for the 3 different choices $\overline{h}_U$ (red dashed line, 2D plane strain), $\overline{h}_U^{3D}$ (blue solid line, 3D penny-shaped without plate corrections) and $\overline{h}_U^S$ (green dashed-dotted line, 3D with approximate plate corrections). For this plot, χ is assumed to be 1 so that $\Delta p_{in} \approx 0.87$ MPa.

non-linear, with transition occurring at much larger L/H than in Equation (56), the first approach to addressing this problem would be more appropriate. However, with this definition of $\overline{h}_U^S$, we can invoke a similar procedure as was suggested in Section 3.1 and simply replace $\overline{h}_U$ with $\overline{h}_U^S$ in all expressions (Equations (42), (43), (46), (50), and (54)), and otherwise use the same self-similar solution. We note that the form of the displacement profile is not expected to stay the same but, as we have no other plausible solution to rely on, we use the same displacement profile and assume that the primary effect of including plate theory is the scaling accounted for by $\overline{h}_U^S$. It can also be noted that the eventual strong dependence of $\overline{h}_U^S$ on L (to the 4th power) implies large vertical displacements for moderately large values of L in this model relative to the crack models (for the same pressure distribution). See Figure 9 for a comparison of vertical displacements calculated for the 3 different choices $\overline{h}_U$, $\overline{h}_U^{3D}$ and $\overline{h}_U^S$ (with numerical values chosen as in Section 3).

3.1.5. Accounting for Pressure Loss to the Bed

[39] In the estimates of crack growth in the first paragraph of Section 3, we estimate the excess pressure at the crack inlet, Δp_{in}, using the hydrostatic excess pressure value, Δp_{static}. However, in Appendix D in Text S1, we show that the loss of pressure (in excess of hydrostatic ice pressure) due to flow from the surface to the base, Δp_{loss}, is a significant fraction (67%) of Δp_{static}.

[40] To account for this pressure loss in the connecting conduit, we no longer set $\Delta p_{in} = \Delta p_{static}$ but instead let $\Delta p_{in} \equiv \chi \Delta p_{static}$, where $0 \leq \chi \leq 1$. In Appendix D in Text S1, we show that χ and U_{vert} (the average fluid velocity in the vertical crack) can be solved for simultaneously. In the late stages of crack growth, when the surface lake is gone but there remains excess water pressure driving the basal crack open, the analysis must be modified to account for this different regime but χ and U_{vert} can still be determined.

3.1.6. Summary of Approximate Models for Comparison With Observations

[41] With the results of Appendix D in Text S1 implemented for determining χ, we now obtain 3 different pre-liminary models as follows. The $\overline{h}_U$ in Equations (46), (50) and (D8) is taken to be one of the 3 choices $\overline{h}_U$, $\overline{h}_U^{3D}$ or $\overline{h}_U^S$, with results for these 3 choices henceforth labeled 'Model I' (using $\overline{h}_U$), 'Model II' (using $\overline{h}_U^{3D}$) and 'Model III' (using $\overline{h}_U^S$), as described in detail in the following 3 paragraphs.

[42] 'Model I': Model I uses average opening $\overline{h}_U$ of Equation (41) of the plane strain solution for crack length $2L$, and adopts the same average over a lateral distance in the y direction that scales with L such that the basal crack volume is given by Equation (54) with $\overline{h}_U$ substituted for $\overline{h}_U^{3D}$. This model neglects that L/H may be of order 1 or larger.

[43] 'Model II': Model II reinterprets the plane strain crack opening solution for a penny-shaped crack of radius L with average opening $\overline{h}_U^{3D}$ of Equation (53), and basal crack volume given by Equation (54). This model also neglects that L/H may be of order 1 or larger.

[44] 'Model III': Model III is the same as 'Model II' except that it uses an approximate implementation of elastic plate bending theory to account for L/H of order 1 or larger. Average opening is estimated by $\overline{h}_U^S$ of Equation (56), and basal crack volume is given by Equation (54) with $\overline{h}_U^S$ substituted for $\overline{h}_U^{3D}$.

[45] Note that since all 3 models combine a 2D approximation for surface displacements (Equation (50)) with a 3D approximation for volumes (Equation (54)), all are hybrid models that should not be expected to precisely agree with any realistic situation.

3.2. Comparison of Model Results With Greenland Observations

[46] We now compare our preliminary model results for crack growth, surface displacements, and corresponding surface-lake water-level time series with the recent observations of rapid surface-lake drainage in Greenland by *Das et al.* [2008]. All displacements plotted are for the observation site at the surface and roughly 1.7 km removed from the center of the connecting conduit ($x_0 = 1.7$ km) (see Figure 1).

[47] The surface displacements used are those calculated by the line source solution of Equation (50) for the vertical uplift (as a function of L) and by the plane stress approximation of Equation (51) for horizontal displacement (as a function of a). In Equation (50), we use either $\overline{h}_U$, $\overline{h}_U^{3D}$ or $\overline{h}_U^S$ as discussed in Section 3.1, giving us solutions for 'Model I', 'Model II', and 'Model III' respectively. (Plots of these displacements as a function of L can be found in the work of *Tsai* [2009].)

[48] As discussed in Appendix D in Text S1, displacements for $L \lesssim 1.7$ km are overestimated (but are nearly negligible anyway). The strong (negative power) dependence of χ on L for 'Model III' implies very small basal excess pressures ($\Delta p_{in} = \chi \Delta p_{static}$) and hence small horizontal displacements for large values of L, and therefore cannot achieve the meter-scale displacements observed [*Das et al.*, 2008]. The very low values of χ attained also imply very low fluid velocities in the basal crack, which eventually leave the turbulent regime that this work is based upon. Thus, 'Model III' (which includes plate corrections) results may not be realistic and this should be kept in mind when interpreting the results for this case. 'Model III' may also be
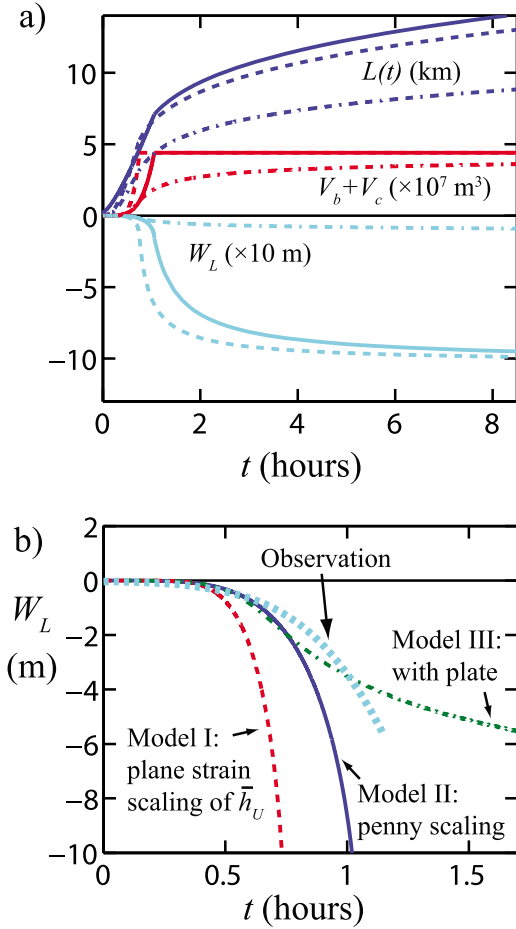
Figure 10. (a) Modeled basal crack length $L(t)$, total crack system volume $V_b + V_c$ and water level W_L for Models I, II and III. The dashed lines denote the 'Model I' results, the solid lines denote the 'Model II' results, and the dashed-dotted lines denote the 'Model III' results. The colors, as labeled, are for $L(t)$ (blue), $V_b + V_c$ (red), and W_L (cyan, below the zero line). (b) Modeled W_L compared against the observed W_L. The red dashed line is the 'Model I' prediction, the blue solid line is the 'Model II' prediction, the green dashed-dotted line is the 'Model III' prediction, and the thick cyan dotted line is the observed W_L. The observation times have been shifted so that the water level begins to drop around $t = 0$.

unrealistic due to the complete vertical crack closure discussed in Appendix D in Text S1.

[49] The observed horizontal displacements (with a maximum of about 0.8 m) are approximately 25% smaller than the observed vertical displacements (with a maximum of about 1.1 m) [*Das et al.*, 2008], and this general behavior is achieved for a range of plausible a/L in both 'Model I' ($\bar{h}_U$) and 'Model II' ($\bar{h}_U^{3D}$). In 'Model I', $0.8 \lesssim a/L \lesssim 1.0$ approximately satisfy this condition. In 'Model II', $0.5 \lesssim a/L \lesssim 0.7$ approximately satisfy this condition. For 'Model III', no range of a/L yields comparable behavior, but higher values ($a/L \gtrsim 0.8$) agree better. For the results shown below, we choose $a/L = 1.0$ for 'Model I', $a/L = 0.6$ for 'Model II', and $a/L = 1.0$ for 'Model III'. We note that we may expect a/L to remain roughly constant throughout

crack growth since the size of the basal crack is the limiting factor on the growth of the vertical connecting conduit.

[50] In our 3 preliminary models, given the basal crack length L at a given time, we can calculate the basal crack growth rate $dL/dt \equiv U_{tip}$ from Equation (46), the basal crack input pressure $\Delta p_{in} = \chi \Delta p_{static}$ from Equations (D12) and (D14), the crack volumes from Equation (D1), and the surface displacements from Equations (50) and (51). Using the instantaneous $dL/dt = U_{tip}$ to step forward in time (i.e. assuming quasi-static crack growth), we can therefore integrate in time to obtain $L(t)$ given only knowledge about the initial lake volume and an initial small crack length L_0. If we also assume a lake geometry, we can additionally calculate the drop in water level in the surface lake (and vertical crack) by equating lake water volume loss to the water volume stored in the crack system (Equation (D1)). Thus, for model input, we take the initial lake volume of $V_0 = 4.4 \cdot 10^7$ m^3, initial lake area of $A_0 = 5.6 \cdot 10^6$ m^2 [*Das et al.*, 2008], and assume the lake to have a paraboloid shape. We do not model the very end of the drainage event, when we expect water in the basal crack to drain into the subglacial hydraulic system and eventually result in zero net displacement. The decrease of $\chi_0 \rightarrow 0$ at these late times also implies much lower fluid velocities, which eventually no longer satisfy the fully turbulent ($\Re \gtrsim 10^5$) approximation used throughout this work.

[51] The model results for Models I, II and III are shown in Figures 10 and 11 as a function of time. Figure 10a shows the crack length $L(t)$, the total volume in the basal crack plus vertical crack $V_b(L(t)) + V_c(a(t))$, and the water level in the lake $W_L(t)$. As discussed earlier, the volume is capped at V_0, after which crack growth changes from using the χ of Equation (D12) to that of Equation (D14) and is responsible for the inflection points in L and W_L as V_0 is reached. When the lake is empty, W_L refers to the remaining water level in the vertical crack ($H_w - H$). Note that the quantities are plotted in different units so as to fit on the same graph. In Figure 10b is a comparison of the modeled W_L of Figure 10 a with the observed W_L of *Das et al.* [2008]. Since the model starting time is arbitrary, we have adjusted the observation times so that the water level begins to drop around $t = 0$. As shown, 'Model I' (with $\bar{h}_U$) has a similar curvature to the observed W_L but is about 40% too fast, 'Model II' (with $\bar{h}_U^{3D}$) is about 20% too fast, and 'Model III' (with $\bar{h}_U^S$) initially follows 'Model II' but then becomes worse as the plate terms have larger contributions ($L \gtrsim H$) (and does not finish draining the lake in the 8-hr timespan plotted, an unrealistic behavior due to the rapid cutoff of the vertical conduit as discussed previously). Figure 11a shows the vertical and horizontal displacements of the same models. The cusps occur when the volume $V_b + V_c$ reaches V_0. In Figure 11b, we compare the modeled displacements with the observed displacements of *Das et al.* [2008]. As shown, 'Model I' again has a timescale about 40% too fast and predicts amplitudes about a factor of 2 too small, 'Model II' again is about 20% too fast and predicts amplitudes slightly worse than 'Model I', and 'Model III' does not predict timescales or amplitudes well. We reiterate that 'Model III' may not capture the transition from $L \ll H$ to $L \gg H$ in a realistic way, and further work must be done to test the validity of the approximation.
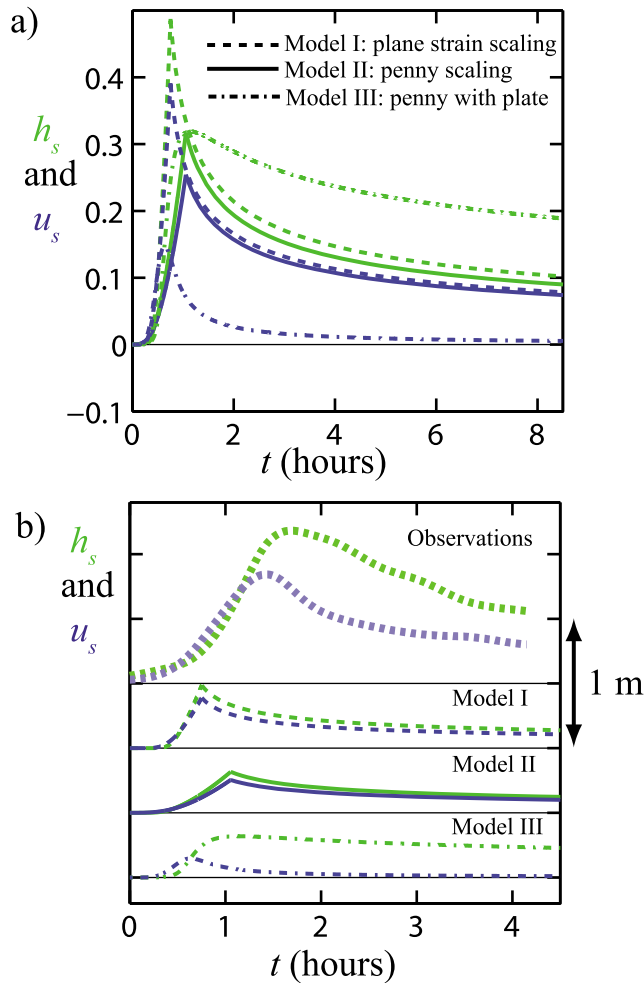
Figure 11. (a) Modeled vertical displacements h_s and horizontal displacements u_s for Models I, II and III. The dashed lines denote the 'Model I' results, the solid lines denote the 'Model II' results, and the dashed-dotted lines denote the 'Model III' results. The colors, as labeled, refer to vertical (green) and horizontal (blue) displacements. (b) Modeled h_s and u_s compared against the observed quantities (thick dotted curves). Here, the curves are offset (by 0.5 m) for clarity. The colors are the same as in Figure 11a.

[52] Displacements in the along-flow direction are not modeled explicitly, but our model predicts complete loss of basal resistance over the basal crack area while the basal crack is in existence and is thus consistent with the observed increase in steady flow toward the Greenland coast during the transient basal crack lifetime. We note that complete crack opening with sheet-like water flow, as in our model, is expected for the entire duration that water pressures are above hydrostatic. (Our model does not attempt to treat the later situation when water pressures are below hydrostatic.) If we take $L \approx 10$ km as the maximum basal crack length, which is achieved long after the peak displacements occur (see Figures 10 and 11), and take the initial average basal shear stress to be $\tau_{b0} \approx 10^5$ Pa [Bamber et al., 2001] then the loss of basal shear force can be approximated as $3 \cdot 10^{13}$ N. This loss of basal shear force could plausibly account for the

observed factor of 3 increase in background flow velocities for the day following the observed drainage [Das et al., 2008], though additional modeling would need to be done to verify this claim. Although also not explicitly modeled, we expect seismicity when strain rates are high and therefore over the full timescale of basal crack growth, not just the timescale of initial lake drainage, which is consistent with the observed seismicity [Das et al., 2008].

3.3. Complications in Comparison With Greenland Observations

[53] In the preceding sections, a very simplified approach was taken in which we considered the approximate elastic response of ice coupled to the turbulent flow of water through a connecting and basal crack. In this analysis, a large number of complicating factors were ignored and here we comment on some of the perhaps more important of these issues.

[54] As discussed above, although we use them outside the known range of applicability, the self-similar results strictly apply only when $L \ll H$. Our attempt at modifying the solution to approximately account for plate theory corrections when $L \gtrsim H$ did not successfully predict observations better than the models without a plate term added. However, since the true mechanics is more complex than the approximate corrections suggested, it would be useful to account for this more properly and hence obtain a solution that is accurate in all regimes of L/H. As an example of an improvement that would result is that the stresses from such a solution should yield larger horizontal surface displacements [Higashida and Kamada, 1982] (as needed to fit observations). It may be possible to construct such a solution using the bimaterial crack approach of Erdogan et al. [1973], Higashida and Kamada [1982], and Hutchinson and Suo [1992] or the matched asymptotic approach of Bunger and Detournay [2005]. We leave this important problem for future work.

[55] Perhaps the next most significant simplification is that of an elastic ice medium. It is well known that glacier ice displays viscous properties [e.g., Paterson, 2002; Hooke, 2005] and should be modeled as a viscoelastic material on timescales close to the Maxwell time (ratio of effective viscosity to elastic stiffness) for glacier ice, which is plausibly in the hour to few hours range [e.g., Tsai et al., 2008]. The fact that the full timescale of interest (a few hours) may be longer than the Maxwell time suggests that the analysis described here is not completely realistic, and may explain why our predicted displacements are smaller than observed (as there would be added viscous strains on top of the elastic strains calculated). This shortcoming of the model is a serious one that we hope to deal with in future work. Nevertheless, the fact that the Maxwell time is not vastly shorter than the process timescale and that there is rough agreement between model and observation suggests that there is merit to the fully elastic approximation. The elastic approximation should, in any event, be valid near the moving rupture front where the timescale of substantial stress changes is much shorter.

[56] In addition to not accounting for viscous effects, the only fractures accounted for are those of the vertical connecting crack and the basal crack. In reality, numerous small fractures might be expected to open and close as the ice

deforms, both due to brittle straining [e.g., *Schulson*, 2001] and due to small-scale hydrofracturing (during crack growth). For example, the positive excess pressures over most of the basal crack favor small scale hydrofracturing upwards into the ice, whereas the strongly negative pressure near the crack tips should encourage the opening of nearby horizontal fractures. The small upwards hydrofractures would be more likely where the largest extensional stresses are. Both small-scale hydrofracturing and brittle straining would contribute to effectively large-scale viscous deformation and would have associated seismicity. This would be consistent with the observed seismicity [*Das et al.*, 2008] and therefore would be useful to have explicitly accounted for in future work. Moreover, this work assumes all of the lake water drains into the two large cracks, without leaking off into any conduits or other hydraulic network. As commented on previously, this is not expected to be a good approximation at the end of drainage. It also may not be a good approximation if there exist large conduits surrounding the crack system prior to the rapid drainage, or if there are layers of weak englacial ice which water could infiltrate.

[57] We also do not account for entrainment of any significant amounts of till (or ice) fragments in the basal flow channel, which may have an effect on the form of the fluid resistance, Equation (1) [see, e.g., *Roberts*, 2005]. Using the Shields criterion [see, e.g., *Buffington*, 1999] to estimate the size of the largest entrained grain fragments D^*, then

$$D^* = \frac{\tau}{\tau_c^*(\rho_s - \rho)g}, \tag{57}$$

where τ_c^* is the dimensionless critical Shields stress and ρ_s is the grain density. For fully turbulent flow, τ_c^* is approximately given by $\tau_c^* \approx 0.045$ [*Lamb et al.*, 2004]. Using the self-similar solution with $\Delta p_{in} = \chi(\rho - \rho_{ice})gH$, we can then estimate τ using Equations (1) and (2), and find

$$D^* = \frac{f_0 \rho U^2}{8\tau_c^*(\rho_s - \rho)g} \cdot \left(\frac{k}{h}\right)^{1/3}$$
$$\approx 9.07 \cdot \frac{\chi^2(\rho - \rho_{ice})^2 gH^2}{(\rho_s - \rho)E'} \cdot \hat{U}(\hat{x})^2 \left(\frac{\hat{w}(0)}{\hat{w}(\hat{x})}\right)^{1/3}, \tag{58}$$

where $\hat{w}(\hat{x})$ and $\hat{U}(\hat{x})$ are shown in Figures 6b ($\hat{w}$ corresponds to $\hat{w}_{self\text{-}sim}$ there) and 7. Thus, with $\chi = 1$, other variables as before, and $\rho_s/\rho \approx 2.7$, then even at $x = 0$ where D^* is smallest, any grains smaller than $D^* \approx 10$ cm would be entrained, leading to a larger τ than used throughout this paper. This underestimate of τ (and therefore of f) may also help to explain the disagreement between our model results and the *Das et al.* [2008] observations. It may also be of interest to note that D^* scales with H^2 and is independent of L at the basal crack inlet ($x = 0$), implying great erosional power of draining surface waters from thick glaciers (e.g., a 2 km glacier would entrain all grains smaller than ≈ 40 cm) regardless of basal crack length.

[58] In our analysis, we also determine pressures and displacements based on 2D plane strain and plane stress approximations, but then modify these solutions for use in a 3D penny-shaped crack. However, future work should be done to verify the validity of this modification procedure. The basal crack is also assumed to be perfectly horizontal, neglecting any bed slope relative to the pressure head gra-

dient. If bed slopes are significant, we would expect the crack to favor propagation in the down-slope direction.

[59] Another important simplification is that we assume no melting or freezing of the ice and liquid water flowing through the cracks. The heating rate (per unit area) due to the turbulent flow τU can be estimated as $f_0 \rho U^3 \approx 10^2$ J m^{-2} s^{-1}, which would only melt warm ice by ≈ 1 mm/hr (since the latent heat of water is $3 \cdot 10^5$ J/kg). Thus, no melting or freezing is a reasonable approximation as long as the thermal diffusion timescale is longer than the process time of a few hours. This diffusion timescale is given by $\tau_d = l^2/\kappa$ where l is the conductive length scale and κ is thermal diffusivity. With $\kappa \approx 10^{-6}$ m^2/s [*Hooke*, 2005] then for $l \gtrsim 10$ cm, $\tau_d \gtrsim 2$ hrs. While it is not clear what range of conductive length scales exist through the crack system, it may be a reasonable guess that $l > 10$ cm, in which case melting and freezing is not important over the timescale of interest. We additionally ignore any instabilities in melting and freezing that might lead to fingering features at the crack front (e.g., as in the work of *Walder* [1982] or *Tsai and Wettlaufer* [2007]). Such short wavelength features are not expected of 3D crack growth without any melting [*Rice*, 1985].

4. Discussion

[60] The results of this work fall naturally into two main parts. In the first part (Section 2), we present a general model for fully turbulent hydraulic fracture, and present solutions under the assumption of either steady state or self-similar crack growth. To our knowledge, this is the first analysis of hydraulic fracture in which the fluid flow is assumed to be fully turbulent ($\Re \gtrsim 10^5$) and the solution obtained is consistent with this turbulent flow. (*Lister and Kerr* [1991] discuss a model for weakly turbulent flow, using a smooth-pipe Blasius approximation applicable to $4 \cdot 10^3 \lesssim \Re \lesssim 10^5$.) Our self-similar solution for crack growth (e.g. Equations (36)–(38)) therefore scales with physical parameters in a distinctly different manner as compared with self-similar solutions with Newtonian viscous flow [*Spence and Sharp*, 1985] or power law fluid flow [*Adachi and Detournay*, 2002]. Since all three of these cases assume a linear elastic medium around the crack, the scalings for crack opening with pressure and crack length are the same, e.g. with Equation (38) depending linearly on crack length (L) multiplied by the ratio of pressure (Δp_{in}) to elastic modulus (E'). However, due to differences in the flow regime assumed, the scalings for crack tip velocity (U_{tip}) are very different. For example, *Spence and Sharp* [1985] show that, in the Newtonian viscous case, a self-similar solution in which Δp_{in} is constant can be achieved for an exponential increase in flow rate ($Q_{2D} \propto e^{ct}$) but not for a situation in which flow rate has a power law dependence ($Q_{2D} \propto t^c$), whereas our turbulent solution has prescribed constant inlet pressure Δp_{in} and has $Q_{2D} \propto t^{7/5}$. This prediction of flow rate, or equivalently of crack growth rate, cannot be made from quasi-static solutions like those of *Weertman* [1973] or *van der Veen* [2007] in which flow rate is treated as a given rather than as a quantity to be solved for in a self-consistent manner. It may also be noted that the turbulent hydraulic fracture results of Section 2 may be useful regardless of the validity or merit of the following

sections in which we attempt to apply the model a lake drainage event in Greenland.

[61] The second main part of this work (Section 3) focuses on a scheme for applying the turbulent hydraulic fracture model of Section 2 to model the rapid drainage of a meltwater lake in Greenland, as recently observed by *Das et al.* [2008]. In utilizing the idealized model of Section 2, a number of approximations are necessarily taken and the limitations of these approximations have been discussed in Section 3.3. This model of meltwater lake drainage makes quantitative predictions of the dynamic growth of the basal crack as well as approximate surface displacements and water drainage rate associated with this growth. In comparison, *Krawczynski et al.* [2009] also model the turbulent flow of water through a vertical crack but use the observed drainage rate to constrain the vertical crack geometry and do not consider the effects of basal crack growth. Moreover, *Krawczynski et al.* [2009] do not attempt to model the growth of the crack system, but instead focus on determining the volume of water necessary for the crack to grow to the base of the ice sheet. The modeling of *van der Veen* [2007] also does not attempt to determine the growth rate of either the vertical or basal crack under the realistic conditions of approximately constant excess pressure Δp_{in}. The work of *Weertman* [1971b] also considers a case of turbulent flow driving crack opening but does not use a crack opening and pressure distribution that are consistent with the fluid flow equations, and therefore does not arrive at a realistic prediction of crack growth [*Stevenson*, 1982]. To our knowledge, *Weertman* [1971b], *van der Veen* [2007], *Krawczynski et al.* [2009] and the present work encompass all of the work done so far in attempting to model rapid meltwater lake drainage events. As such, although our model results are preliminary and have much room for improvement, they are the only ones capable of quantitative predictions of crack growth rates, drainage rates, and surface displacements associated with the drainage.

5. Conclusions

[62] We have presented a general model in which turbulent flow of water drives open a fracture within a purely elastic medium. We find that given certain assumptions about physical parameters, we can calculate the crack-tip speed as well as the pressure and displacement profiles along the crack. We present a steady state solution and a self-similar solution (both with $L \ll H$). We then apply the self-similar results to the case of a surface lake draining to the base of the Greenland Ice Sheet. Despite needing to use the models beyond their known range of validity (e.g., for $L \gtrsim H$), we nonetheless find that our models can be constructed to have order of magnitude agreement with the observations of *Das et al.* [2008]. Our preliminary prediction is of basal crack growth eventually up to a radius of 5–10 km, with lake water-level predictions matching observations to within 20–40%, but with predicted surface displacements a factor of 2–3 smaller than observed. The inclusion of additional complexity, such as viscous creep and a more realistic treatment of the whole range of L/H, may help yield model results in better agreement between the observations, and we suggest possible directions for future work.

Notation

A constant related to U_{tip} in equation (13).
A' constant related to A.
A_k self-similar series constants.
a half-length of connecting conduit.
b distance along crack of force pair.
C_1 $h_{avg}/\overline{h}_U$.
C_2 scaling factor for velocity in equation (46).
c_0 coefficient in lubrication equation.
c_k constants chosen to satisfy $K_{Ic} = 0$.
D self-similar series constant.
$D*$ size of largest entrained grains.
E Young's modulus.
E' effective modulus in plane strain.
E_{loss} energy loss.
e_{loss} energy loss per unit area.
F_{ij} angular function associated with σ_{ij}.
$F(\hat{x})$ pressure term associated with first term of self-similar opening series.
f Darcy-Weisbach friction factor.
f_0 value of f at reference scale.
G shear modulus.
g gravitational acceleration.
$g(z), F(z)$ complex bimaterial functions.
H height of ice sheet.
H_w height of water.
h basal crack opening.
h_0 crack opening estimate.
h_{avg} average value of h.
h_s surface uplift from crack opening.
h_s^V surface uplift from V_c crack.
h_U^P opening of plate for uniform p.
$\overline{h}_U$ average opening for uniform p.
$\overline{h}_U^{3D}$ average opening for 3D uniform p.
$\overline{h}_U^P$ average opening of plate for uniform p.
$\overline{h}_U^S$ average opening of 3D crack plus plate.
I_k integral expressions.
K_I stress intensity factor.
K_{Ic} fracture toughness.
k Nikuradse roughness height.
L horizontal basal crack length.
$\hat{L}$ non-dimensional L.
L_0 characteristic scale for L.
L_c surface crack length.
LHS left-hand side of equation (26).
l conductive length scale.
m power law index.
n Manning roughness.
P constant in equation (13).
p fluid pressure in crack.
Δp pressure in excess of hydrostatic.
$\hat{p}$ non-dimensional Δp.
Δp_0 characteristic scale for Δp.
Δp_{in} excess pressure at crack inlet.
Δp_{hy} hydrostatic component of Δp_{in}.
Δp_{static} Δp from column of standing water.
Δp_{loss} loss of pressure in excess of hydrostatic.
Q_{2D} 2D flow rate.
Q_b flow rate contributed by V_b.
Q_c flow rate contributed by V_c.

q constant in complex potential.

R distance along crack behind crack tip.

$\mathcal{R}$ distance from center of 3D crack.

$\hat{\mathcal{R}}$ non-dimensional $\mathcal{R}$.

R_h hydraulic radius.

$\Re$ Reynolds number.

RHS right-hand side of equation (26).

r distance away from crack tip.

S negative hydraulic head gradient.

$s, \hat{s}$ dummy variables.

T timescale of drainage.

t time.

$\hat{t}$ non-dimensional t.

U fluid velocity averaged across h.

$\hat{U}$ non-dimensional U.

U_0 characteristic scale for U.

$U_{Manning}$ Manning velocity.

U_{vert} average velocity in vertical conduit.

U_{tip} crack-tip velocity.

u_{P1} horizontal displacement due to force pair.

u_s surface horizontal displacement.

$u + iv$ complex displacement.

V_0 initial lake volume.

V_{2D} 2D crack volume.

V_b basal crack volume.

V_c connecting crack volume.

W_L water level.

w model crack opening.

$\hat{w}$ non-dimensional w.

w_0 characteristic scale for w.

w_k terms of self-similar opening series.

w_U model opening for uniform p.

w_U^{3D} model opening of 3D crack for uniform p.

x horizontal position along crack.

x_0 horizontal sensor position.

y vertical position.

z complex variable.

α, β, γ self-similar constants.

$\dot{\gamma}$ shear rate.

δ elastic constant relating w and Δp.

ϵ bimaterial mismatch constant.

ϵ_m normalized squared error.

η water viscosity.

η_k $3 - 4\,\nu_k$.

ϕ self-similar constant for velocity scale.

φ dummy variable.

$\phi(z), \psi(z)$ Muskhelishvili potentials.

κ thermal diffusivity.

ν, ν_k Poisson's ratio.

ρ water density.

ρ_{ice} ice density.

ρ_s grain density.

σ_0 hydrostatic ice overburden pressure.

σ_{ij} stress tensor components.

τ average shear stress on channel walls.

τ_{b0} initial basal shear stress.

τ_c^* dimensionless critical Shields stress.

τ_d diffusion timescale.

θ angle around crack tip.

ξ h/w.

χ $\Delta p_{in}/\Delta p_{hy}$.

χ_w $\Delta p_{hy}/\Delta p_{static}$.

χ_0 $\chi \cdot \chi_w$.

References

Adachi, J. I., and E. Detournay (2002), Self-similar solution of a plane-strain fracture driven by a power-law fluid, *Int. J. Numer. Anal. Methods Geomech.*, *26*, 579–604, doi:10.1002/nag.213.

Alley, R. B., T. K. Dupont, B. R. Parizek, and S. Anandakrishnan (2005), Access of surface meltwater to beds of sub-freezng glaciers: Preliminary insights, *Ann. Glaciol.*, *40*, 8–14.

Ashby, M. F. (1989), Materials selection in conceptual design, *Mater. Sci. Tech.*, *5*, 517–525.

Bamber, J. L., R. L. Layberry, and S. P. Gogineni (2001), A new ice thickness and bed data set for the Greenland Ice Sheet: 1. measurement, data reduction, and errors, *J. Geophys. Res.*, *106*, 33,773–33,780.

Bilby, B. A., A. H. Cottrell, and K. H. Swinden (1963), The spread of plastic yield from a notch, *Proc. R. Soc. London A*, *272*, 304–314.

Bindschadler, R. A., M. A. King, R. B. Alley, S. Anandakrishnan, and L. Padman (2003), Tidally controlled stick-slip discharge of a West Antarctic ice stream, *Science*, *301*, 1087–1089.

Bird, R. B., R. C. Armstrong, and O. Hassager (1987), *Dynamics of Polymeric Liquids*, vol. 1, 2nd ed., 649 pp., John Wiley, New York.

Buffington, J. M. (1999), The legend of A. F. Shields, *J. Hydraul. Eng.*, *125*, 376–387.

Bunger, A. P., and E. Detournay (2005), Propagation of a penny-shaped fluid-driven fracture in an impermeable rock: asymptotic solutions, *Int. J. Solids Struct.*, *39*, 6311–6337.

Bunger, A. P., and E. Detournay (2008), Experimental validation of the tip asymptotics for a fluid-driven crack, *J. Mech. Phys. Solids*, *56*, 3101–3115.

Clarke, G. K. C. (1996), Lumped-element analysis of subglacial hydraulic circuits, *J. Geophys. Res.*, *101*, 17,547–17,559.

Das, S., I. Joughin, M. D. Behn, I. M. Howat, M. A. King, D. Lizarralde, and M. P. Bhatia (2008), Fracture propagation to the base of the Greenland Ice Sheet during supraglacial lake drainage, *Science*, *320*, 778–781, doi:10.1126/science.1153360.

Desroches, J., E. Detournay, B. Lenoach, P. Papanastasiou, J. R. A. Pearson, M. Thiercelin, and A. Cheng (1994), The crack tip region in hydraulic fracturing, *Proc. R. Soc. London A*, *447*, 39–48.

Detournay, E. (2004), Propagation regimes of fluid-driven fractures in impermeable rocks, *Int. J. Geomech.*, *4*, 35–45.

Dyskin, A. V., L. N. Germanovich, and K. B. Ustinov (2000), Asymptotic analysis of crack interaction with free boundary, *Int. J. Solids Struct.*, *37*, 857–886.

Ekstrom, G., M. Nettles, and V. C. Tsai (2006), Seasonality and increasing frequency of Greenland glacial earthquakes, *Science*, *311*, 1756–1758, doi:10.1126/science.1122112.

Erdogan, F., G. D. Gupta, and T. S. Cook (1973), Numerical solution of singular integral equations, in *Methods of Analysis and Solution of Crack Problems: Recent Developments in Fracture Mechanics*, edited by G. C. Sih, pp. 368–425, Noordhoff, Leyden, Netherlands.

Fischer, M. P., R. B. Alley, and T. Engelder (1995), Fracture toughness of ice and firn determined from the modified ring test, *J. Glaciol.*, *41*, 383–394.

Flowers, G. E., H. Bjornsson, F. Palsson, and G. K. C. Clarke (2004), A coupled sheet-conduit mechanism for jokulhlaup propagation, *Geophys. Res. Lett.*, *31*, L05401, doi:10.1029/2003GL019088.

Fricker, H. A., T. Scambos, R. Bindschadler, and L. Padman (2007), An active subglacial water system in West Antarctica mapped from space, *Science*, *315*, 1544–1548, doi:10.1126/science.1136897.

Garagash, D. I., and E. Detournay (2005), Plane-strain propagation of a fluid-driven fracture: Small toughness solution, *J. Appl. Mech.*, *72*, 916–928.

Gioia, G., and P. Chakraborty (2006), Turbulent friction in rough pipes and the energy spectrum of the phenomenological theory, *Phys. Rev. Lett.*, *96*, 044502, doi:10.1103/PhysRevLett.96.044502.

Higashida, Y., and K. Kamada (1982), Stress fields around a crack lying parallel to a free surface, *Int. J. Fracture*, *19*, 39–52.

Hooke, R. L. (2005), *Principles of Glacier Mechanics*, 2nd ed., 429 pp., Cambridge Univ. Press, New York.

Hutchinson, J. W., and Z. Suo (1992), Mixed mode cracking in layered materials, in *Advances in Applied Mechanics*, vol. 29, edited by J. W. Hutchinson and T. Y. Wu, pp. 63–191, Academic, San Diego, Calif.

Jellinek, H. H. G., and R. Brill (1956), Viscoelastic properties of ice, *J. Appl. Phys.*, *27*, 1198–1209.

Joughin, I., I. Howat, R. B. Alley, G. Ekstrom, M. Fahnestock, T. Moon, M. Nettles, M. Truffer, and V. C. Tsai (2008), Ice-front variation and tidewater behavior on Helheim and Kangerdlugssuaq glaciers, Greenland, *J. Geophys. Res.*, *113*, F01004, doi:10.1029/2007JF000837.

Kenneally, J. P. (2003), Crevassing and calving of glacial ice, Ph.D. thesis, Univ. of Maine, Orono.

Krawczynski, M. J., M. D. Behn, S. B. Das, and I. Joughin (2009), Constraints on lake volume required for hydro-fracture through ice sheets, *Geophys. Res. Lett.*, *36*, L10501, doi:10.1029/2008GL036765.

Lamb, M. P., W. E. Dietrich, and J. G. Venditti (2004), Is the critical Shields stress for incipient sediment motion dependent on channel-bed slope?, *J. Geophys. Res.*, *113*, F02008, doi:10.1029/2007JF000831.

Lister, J. R. (1990), Buoyancy-driven fluid fracture: the effects of material toughness and of low-viscosity precursors, *J. Fluid Mech.*, *210*, 263–280.

Lister, J. R., and R. C. Kerr (1991), Fluid-mechanical models of crack propagation and their application to magma transport in dykes, *J. Geophys. Res.*, *96*, 10,049–10,077.

Manning, R. (1891), On the flow of water in open channels and pipes, *Trans. Inst. Civil Eng.*, *20*, 161–207.

Mendelsohn, D. A. (1984), A review of hydraulic fracture modeling, part I: General concepts, 2D models, motivation for 3D modeling, *J. Energy Resour. Technol.*, *106*, 369–376.

Muskhelishvili, N. I. (1953), *Some Basic Problems of the Mathematical Theory of Elasticity: Fundamental Equations, Plane Theory of Elasticity, Torsion, and Bending*, 3rd ed., 704 pp., Noordhoff, Groningen, Netherlands.

Ng, F., and H. Bjornsson (2003), On the Clague-Matthews relation for jokulhlaups, *J. Glaciol.*, *49*, 161–172.

Nye, J. F. (1976), Water flow in glaciers: Jokulhlaups, tunnels and veins, *J. Glaciol.*, *17*, 181–205.

Paterson, W. S. B. (2002), *The Physics of Glaciers*, 3rd ed., 481 pp., Elsevier, New York.

Rice, J. R. (1985), First-order variations in elastic fields due to variation in location of a planar crack front, *J. Appl. Mech.*, *52*, 571–579.

Rist, M. A., P. R. Sammonds, S. A. F. Murrell, P. G. Meredith, C. S. M. Doake, H. Oerter, and K. Matsuki (1999), Experimental and theoretical fracture mechanics applied to antarctic ice fracture and surface crevassing, *J. Geophys. Res.*, *104*, 2973–2987.

Roberts, M. J. (2005), Jokulhlaups: A reassessment of floodwater flow through glaciers, *Rev. Geophys.*, *43*, RG1002, doi:10.1029/2003RG000147.

Roper, S. M., and J. R. Lister (2007), Buoyancy-driven crack propagation: the limit of large fracture toughness, *J. Fluid Mech.*, *580*, 359–380, doi:10.1017/S0022112007005472.

Rothlisberger, H. (1972), Water pressure in intra- and subglacial channels, *J. Glaciol.*, *11*, 177–203.

Rouse, H. (1955), *Elementary Mechanics of Fluids*, 9th ed., 376 pp., John Wiley, New York.

Rubin, A. M. (1995), Propagation of magma-filled cracks, *Annu. Rev. Earth Planet. Sci.*, *23*, 287–336.

Rubin, H., and J. Atkinson (2001), *Environmental Fluid Mechanics*, 728 pp., Marcel Dekker, New York.

Savitski, A. A., and E. Detournay (2002), Propagation of a penny-shaped fluid-driven fracture in an impermeable rock: asymptotic solutions, *Int. J. Solids Struct.*, *39*, 6311–6337.

Schulson, E. M. (2001), Brittle failure of ice, *Eng. Fract. Mech.*, *68*, 1839–1887.

Schulson, E. M., and P. Duval (2009), *Creep and Fracture of Ice*, 416 pp., Cambridge Univ. Press, Cambridge, U. K.

Smith, R. A. (1976), The application of fracture mechanics to the problem of crevasse propagation, *J. Glaciol.*, *76*, 223–228.

Sneddon, I. N. (1946), The distribution of stress in the neighbourhood of a crack in an elastic solid, *Proc. R. Soc. London A*, *187*, 229–260.

Spence, D. A., and P. Sharp (1985), Self-similar solutions for elastohydrodynamic cavity flow, *Proc. R. Soc. London A*, *400*, 289–313.

Stevenson, D. J. (1982), Migration of fluid-filled cracks: Applications to terrestrial and icy bodies, *Lunar Planet. Sci.*, *XIII*, Abstract 1394.

Strickler, A. (1923), Beitrage zur frage der geschwindigkeitsformel und der rauhigkeitszahlen fur strome, kanale und geschlossene leitungen, *Tech. Rep. 16*, Mitteilungen des Eidgenossischen Amtes fur Wasserwirtschaft, Bern.

Strickler, A. (1981), Contributions to the question of a velocity formula and roughness data for streams, channels and closed pipelines, Rep. T-10, Translated from German by T. Roesgen et al., Lab. of Hydraul. and Water Resour., Calif. Inst. of Technol., Pasadena.

Tada, H., P. C. Paris, and G. R. Irwin (2000), *The Stress Analysis of Cracks Handbook*, 3rd ed., 677 pp., ASME Press, New York.

Timoshenko, S. P., and J. N. Goodier (1987), *Theory of Elasticity*, 3rd ed., 567 pp., McGraw-Hill, New York.

Tsai, V. C. (2009), The use of simple physical models in seismology and glaciology, Ph.D. thesis, Harvard Univ., Cambridge, Mass.

Tsai, V. C., and J. S. Wettlaufer (2007), Star patterns on lake ice, *Phys. Rev. E*, *75*, 066105, doi:10.1103/PhysRevE.75.066105.

Tsai, V. C., J. R. Rice, and M. Fahnestock (2008), Possible mechanisms for glacial earthquakes, *J. Geophys. Res.*, *113*, F03014, doi:10.1029/2007JF000944.

van der Veen, C. J. (1998), Fracture mechanics approach to penetration of surface crevasses on glaciers, *Cold Reg. Sci. Technol.*, *27*, 31–47.

van der Veen, C. J. (2007), Fracture propagation as means of rapidly transferring surface meltwater to the base of glaciers, *Geophys. Res. Lett.*, *34*, L01501, doi:10.1029/2006GL028385.

Vaughan, D. G. (1995), Tidal flexure at ice shelf margins, *J. Geophys. Res.*, *100*, 6213–6224.

Walder, J. S. (1982), Stability of sheet flow of water beneath temperate glaciers and implications for glacier surging, *J. Glaciol.*, *28*, 273–293.

Weertman, J. (1971a), Theory of water-filled crevasses in glaciers applied to vertical magma transport beneath oceanic ridges, *J. Geophys. Res.*, *76*, 1171–1183.

Weertman, J. (1971b), Velocity at which liquid-filled cracks move in the Earth's crust or in glaciers, *J. Geophys. Res.*, *76*, 8544–8553.

Weertman, J. (1973), Can a water-filled crevasses reach the bottom surface of a glacier?, *IAHS AISH Publ.*, *95*, 139–145.

White, F. M. (2008), *Fluid Mechanics*, 6th ed., 864 pp., McGraw-Hill, New York.

Wiens, D. A., S. Anandakrishnan, J. P. Winberry, and M. A. King (2008), Simultaneous teleseismic and geodetic observations of the stick-slip motion of an Antarctic ice stream, *Nature*, *453*, 770–774, doi:10.1038/nature06990.

Williams, M. L. (1952), Stress singularities resulting from various boundary conditions in angular corners of plates in extension, *J. Appl. Mech.*, *19*, 526–528.

Zwally, H. J., W. Abdalati, T. Herring, K. Larson, J. Saba, and K. Steffen (2002), Surface melt-induced acceleration of Greenland Ice Sheet flow, *Science*, *297*, 218–222, doi:10.1126/science.1072708.

J. R. Rice, Department of Earth and Planetary Sciences and School of Engineering and Applied Sciences, Harvard University, 29 Oxford St., Cambridge, MA 02138, USA. (rice@seas.harvard.edu)

V. C. Tsai, U.S. Geological Survey, 1711 Illinois St., Golden, CO 80401, USA. (victor.c.tsai@gmail.com)

Text S1

Appendix A: Validity of the Bimaterial Approximation

In Section 2.2, we approximate the bimaterial crack as having an opening given by ξ times the opening for a crack in a homogeneous sample of the more compliant material. Here, we verify the validity of this approximation for an ice-rock interface. Following the analysis of *Rice and Sih* [1965] (see also *England* [1965] and *Erdogan* [1965]), we consider a crack of length $2L$ along the bimaterial interface within an infinite medium with upper medium characterized by shear modulus G_1 and Poisson's ratio ν_1 and lower medium characterized by G_2 and ν_2. For our ice-rock case, we take ice elastic parameters as in Section 3 ($E_1 = 6.2\,\text{GPa}$, $\nu_1 = 0.3$ so that $G_1 = 2.4\,\text{GPa}$) and rock elastic parameters from near-surface granite seismic velocities of *Lay and Wallace* [1995] (and $\rho_2 = 2750\,\text{kg/m}^3$) which give $G_2 = 23\,\text{GPa} \approx 9.6 G_1$ and $\nu_2 = 0.3 \approx \nu_1$. With these choices, the bimaterial 'mismatch' constant

$$\epsilon \equiv \frac{1}{2\pi} \log\left[\left(\frac{\eta_1}{G_1} + \frac{1}{G_2}\right) \Big/ \left(\frac{\eta_2}{G_2} + \frac{1}{G_1}\right)\right], \qquad (A1)$$

with $\eta \equiv 3 - 4\nu$, has a value of $\epsilon = 0.075124$. Given an arbitrary crack pressure loading $P(x)$ along $-L < x < L$, the complex displacements $u_k + iv_k$ (u_k in the horizontal direction and v_k in the vertical direction, throughout this appendix) on either side of the crack ($k = 1$ or 2) are given by Equations (14) and (15) of *Rice and Sih* [1965] (evaluated along $z = \bar{z}$ where $z = z_1 + iz_2$ is a complex variable, with z_1 horizontal and z_2 vertical coordinates) to be

$$2G_1(u_1 + iv_1)$$
$$= \eta_1 \int^z g(s)F(s)ds - e^{2\pi\epsilon} \int^{\bar{z}} g(\bar{s})F(\bar{s})d\bar{s} \qquad (A2)$$

on the upper side and

$$2G_2(u_2 + iv_2)$$
$$= e^{2\pi\epsilon}\eta_2 \int^z g(s)F(s)ds - \int^{\bar{z}} g(\bar{s})F(\bar{s})d\bar{s} \qquad (A3)$$

on the lower side. As also given in *Rice and Sih* [1965],

$$F(z) = (z^2 - L^2)^{-1/2}\left(\frac{z+L}{z-L}\right)^{i\epsilon}, \qquad (A4)$$

with branch cut along the crack such that $zF(z) \to 1$ as $|z| \to \infty$, and

$$g(s) = \int_{-L}^{L} g(s, b)\, db, \qquad (A5)$$

where

$$g(s, b) = \frac{P(b)}{2\pi}\frac{e^{-\pi\epsilon}}{s-b}(L^2 - b^2)^{1/2}\left(\frac{L-b}{L+b}\right)^{i\epsilon}. \qquad (A6)$$

Along the crack face $-L < s < L$, $F(s)$ simplifies to

$$F(s_\pm) = -1 \cdot \pm i e^{\pm\pi\epsilon}(L^2 - s^2)^{-1/2}$$
$$\cdot[\cos(\epsilon \log \frac{L+s}{L-s}) + i\sin(\epsilon \log \frac{L+s}{L-s})], \qquad (A7)$$

where $+$ is used for s above the crack, $-$ is used for s below the crack.

Substituting Equations (A5) and (A7) into Equations (A2) and (A3) gives expressions for the complex displacements along the crack face. Expanding each of these expressions as a power series in the parameter ϵ and approximating the expressions to first order in ϵ (ignoring all higher-order terms, which is appropriate except extremely close to the ends, because of the logarithmic divergence), we find that we can express the complex displacements along the crack face as

$$u_1 + iv_1 = \frac{1}{E_1'}(\epsilon I_1 + iI_2) + O(\epsilon^2) \qquad (A8)$$

and

$$u_2 + iv_2 = -\frac{1}{E_2'}(\epsilon I_1 + iI_2) + O(\epsilon^2). \qquad (A9)$$

I_1 and I_2 are (complicated) expressions that involve only real integrals, and the full crack opening displacement in a homogeneous medium characterized by G_1 and ν_1 is given by

$$2(u_1 + iv_1) = 0 + \frac{1}{E_1'}iI_2. \qquad (A10)$$

We then observe that to order ϵ, the displacement v_1 is unchanged from its value in the homogeneous case and that the displacement on the lower side, v_2 is given by

$$v_2 \approx -\frac{E_1'}{E_2'}v_1 \approx -\frac{v_1}{9.6}. \qquad (A11)$$

Thus, the full opening in the bimaterial case $v_1 - v_2$ is approximately ξ of the full opening in the homogeneous case where ξ is given by

$$\xi \approx \frac{1 + E_1'/E_2'}{2} \approx 0.55. \qquad (A12)$$

We therefore use the approximation $h = 0.55w$.

Appendix B: Stresses in the Bulk

Here, we describe the stresses in the elastic medium associated with the crack-tip solution of *Desroches et al.* [1994] that are used to obtain Equations (12) and (13). Following *Desroches et al.* [1994], we write the *Muskhelishvili* [1953] potential as

$$\phi(z) = \frac{A'}{2q}z^q, \qquad (B1)$$

where $z = z_1 + iz_2$ is again a complex variable, and q is a constant. We follow *Desroches et al.* [1994] and take the other *Muskhelishvili* [1953] potential as $\psi(z) = \phi(z) - z\phi'(z)$ in order to maintain zero shear along the crack axis $y = 0$. We can then calculate the stresses in polar coordinates to be given by

$$\frac{\sigma_{\theta\theta} + \sigma_{rr}}{2} = \frac{\sigma_{xx} + \sigma_{yy}}{2} = A'r^{q-1}\cos[(q-1)\theta] \qquad (B2)$$

and

$$\frac{\sigma_{\theta\theta} - \sigma_{rr}}{2} + i\sigma_{r\theta} = e^{2i\theta} \left(\frac{\sigma_{yy} - \sigma_{xx}}{2} + i\sigma_{yx} \right)$$
$$= (1 - q)A'r^{q-1} \sin(\theta)[-\sin(q\theta) + i\cos(q\theta)]. \qquad (B3)$$

Solving for the stresses gives

$$\sigma_{rr}(r,\theta) = A'r^{q-1}$$
$$\cdot \left[\frac{3-q}{2} \cos[(1-q)\theta] - \frac{1-q}{2} \cos[(1+q)\theta] \right], \qquad (B4)$$

$$\sigma_{r\theta}(r,\theta) = A'r^{q-1}$$
$$\cdot \left[\frac{1-q}{2} \sin[(1-q)\theta] - \frac{1-q}{2} \sin[(1+q)\theta] \right], \qquad (B5)$$

and

$$\sigma_{\theta\theta}(r,\theta) = A'r^{q-1}$$
$$\cdot \left[\frac{1+q}{2} \cos[(1-q)\theta] + \frac{1-q}{2} \cos[(1+q)\theta] \right]. \qquad (B6)$$

These expressions give the stress components of the *Desroches et al.* [1994] solution except for a possible added uniform pressure, $\sigma_{\theta\theta} = -P$ and $\sigma_{rr} = -P$, and an additional added crack-parallel stress $\sigma_{xx} = constant$ (which will not enter our analysis). Equation (13) is then obtained by demanding that $p(x)$ and the crack opening gap satisfy the fluid equations (Equations (7), (9) and (10)) in the case of steady state growth, leading to $q = 2/(2 + m) = 6/7$ and evaluating Equation (B6) along the crack opening to yield

$$\Delta p(x) - P = -\sigma_{\theta\theta}(R, \pi)$$
$$= -A'R^{-1/7} \cos\left(\frac{\pi}{7} \right) = -AR^{-1/7}, \qquad (B7)$$

where $A = A' \cos(\pi/7)$ corresponds to the quantity introduced in Equation (12).

Appendix C: Displacement Calculations

The vertical surface displacements (uplift) due to both cracks are easily calculated using the reciprocal theorem and the Boussinesq-Flamant line-source solution (see e.g. *Timoshenko and Goodier* [1987]). The result, e.g. as in the Appendix of *Walsh and Rice* [1979], is that the vertical surface uplift h_s in a homogeneous half-space due to a vertical opening displacement $w^* = w^*(x)$ of a horizontal surface is

$$h_s(x_0, y_0) = \int_{surf} \sigma_{yy}^*(x - x_0, y - y_0)w^*(x)dx, \qquad (C1)$$

where σ_{yy}^* is given by

$$\sigma_{yy}^* = \frac{2}{\pi} \cdot \frac{(y - y_0)^3}{[(x - x_0)^2 + (y - y_0)^2]^2}, \qquad (C2)$$

and (x_0, y_0) is the uplift location. Applying this to the basal crack, and utilizing the bimaterial approximation for the opening displacement of the crack, $w^* = h(x) \approx w(x)/2$, but ignoring bimaterial effects on Equation (C2), then

$$h_s(x_0) \approx \int_{-L}^{L} \frac{1}{\pi} \cdot \frac{H^3 w(x)}{[(x - x_0)^2 + H^2]^2} dx, \qquad (C3)$$

where variables are as before. Putting this into non-dimensional form and substituting Equation (42) for $\xi w(x)$,

we obtain

$$h_s(x_0) \approx \frac{H^3 \bar{h}_U}{\xi \pi^2 L^3} \int_{-1}^{1} \frac{\hat{w}(\hat{x})\, d\hat{x}}{[(\hat{x} - \hat{x}_0)^2 + \hat{H}^2]^2}, \qquad (C4)$$

where $\hat{H} \equiv H/L(t)$, $\hat{x}_0 = x_0/L(t)$, $\hat{w}(\hat{x})$ is the scaled self-similar opening given in Equation (27), and other variables are as before. Thus, given a surface location x_0 (relative to the crack inlet at $x = 0$ and in the plane of crack growth) and crack length $L(t)$, Equation (50) gives h_s in terms of our self-similar solution.

We can similarly account for the vertical displacement due to the horizontal opening of the vertical crack, and as shown below find that this contribution is negligible. Again as in *Walsh and Rice* [1979], the contribution due to the vertical crack's horizontal displacement u^* is

$$h_s^V = \int_{surf} \sigma_{xx}^* u^* dy, \qquad (C5)$$

where σ_{xx}^* is given for a homogeneous halfspace by

$$\sigma_{xx}^* = \frac{2}{\pi} \cdot \frac{(x - x_0)^2(y - y_0)}{[(x - x_0)^2 + (y - y_0)^2]^2}. \qquad (C6)$$

Applying this to the vertical crack then

$$h_s^V(x_0) \approx \int_0^H \frac{2x_0^2 y u^*(y)\, dy}{\pi(x_0^2 + y^2)^2}. \qquad (C7)$$

Noting that for the observations of *Das et al.* [2008], $x_0/H \approx 1.7$ then this contribution to h_s is bounded by

$$h_s^V(x_0) \leq \int_0^1 \frac{2 \cdot 1.7^2\, \hat{y}\, d\hat{y}}{\pi(1.7^2 + \hat{y}^2)^2} \cdot \max[u^*] = 0.08 \max[u^*]. \quad (C8)$$

Since $\max[u^*]$ is expected to be of similar (or smaller) magnitude to w^*, the contribution h_s^V is thus expected to be an order of magnitude less than that due to the basal crack opening, and we therefore neglect this contribution.

For horizontal surface displacements, we similarly expect an order of magnitude smaller contribution from vertical opening of the basal crack compared to horizontal opening of the (vertical) connecting crack, and hence ignore this former contribution. The horizontal displacement at a distance x_0 perpendicular to the center of the plane stress center crack (see Figure 8) can be obtained by integrating the results of *Tada et al.* [2000] as follows. *Tada et al.* [2000] provides the displacement at x_0 due to a pair of point forces of amplitude P_1 to be

$$u_{P1}(x_0) = \frac{4P_1}{\pi E} \left[\tanh^{-1} \sqrt{\frac{a^2 - b^2}{a^2 + x_0^2}} \right.$$
$$\left. + \frac{1 + \nu}{2} \cdot \frac{x_0^2}{b^2 + x_0^2} \sqrt{\frac{a^2 - b^2}{a^2 + x_0^2}} \right], \qquad (C9)$$

where b is the distance from the center of the crack of the pair of forces. Integrating this expression over the crack face ($0 \leq b \leq a$) gives the corresponding expression, due to a constant pressure Δp_{avg} along the crack, of

$$u_s(x_0) = \frac{2\Delta p_{avg} a}{E} \left[\sqrt{1 + (x_0/a)^2} - (x_0/a) \right.$$
$$\left. + \frac{1 + \nu}{2}(x_0/a)\left(1 - \frac{x_0/a}{\sqrt{1 + (x_0/a)^2}} \right) \right], \qquad (C10)$$

which we take as an approximation to the horizontal surface displacement.

Appendix D: Estimates of Errors and Improvements on Approximations

Here, we first find that the approximations $L \ll H$ and $\Delta p_{loss} \ll \Delta p_{static}$ are of concern. Following estimates of how well these approximations are satisfied, we discuss possible approaches to addressing the two problems.

First, we can make an estimate of how large L becomes by equating the volume of water taken up by the basal crack plus vertical crack ($V_b + V_c$) with the initial volume of water in the surface lake (V_0). The initial lake volume was observed to be $V_0 = 4.4 \cdot 10^7$ m^3 [*Das et al.*, 2008], and we calculate the sum of the crack volumes to be

$$V_b(L) + V_c(a) = \pi \frac{\Delta p_{in}}{E} L^3 \left(\frac{16\xi C_1(1-\nu^2)}{3\pi} + \frac{a^2 H_w}{L^3} \right) \text{(D1)}$$

Choosing $a = L$ as a plausible upper bound on V_c (as discussed in the next paragraph, which results in a lower bound on L) predicts that $L \gtrsim 5.25$ km is reached and thus suggests that the approximation $L \ll H$ should be revisited.

Second, we estimate the pressure loss from turbulent flow en route to the bed by applying the turbulent Manning-Strickler scaling of Equation (6) with each term estimated for flow through the vertical crack. As in our earlier plane stress calculation for this vertical crack, we assume a depth-averaged value of excess pressure $\Delta p_{in}/2$ opening the crack, giving a cross-sectionally averaged opening of $2u_{avg} \equiv \pi u_s(0)/2 \approx \pi \Delta p_{in} a/2E$. We expect that a lies in the range $0.1 \lesssim a/L < 1$ since significant opening will only occur over the region with minimal basal shear stress to counteract the excess pressure (i.e. $a < L$) but for $a \ll L$ the excess pressure should encourage a to grow (i.e. $a \gtrsim 0.1L$). Taking $L \approx 3$ km and $a/L \approx 0.8$ as plausibly representative, then $2u_{avg} \approx 0.48$ m. The average fluid velocity through this vertical crack U_{vert} can be estimated by equating the volumetric flow rate in the vertical crack $\pi a u_s(0) U_{vert} = 4a u_{avg} U_{vert}$ to the volumetric flow rate into the basal crack $dV_b/dt \equiv dV_b/dL \cdot U_{tip}$ (where V_b is given by Equation (54)). Using the procedures of Section 3.1, we estimate dV_b/dt using $\bar{h}_U^{3D}$, which gives $U_{tip} \approx 1.4$ m/s and therefore $dV_b/dt \approx 8.5 \cdot 10^3$ m^3/s. Using these values, then $U_{vert} \approx 3.7$ m/s and the loss of pressure in excess of hydrostatic through the connecting conduit would be

$$\Delta p_{loss} = \frac{0.0357\rho U_{vert}^2 k^{1/3} H}{(2u_{avg})^{4/3}} \approx 0.58 \text{ MPa}, \quad \text{(D2)}$$

which is a large fraction (67%) of the maximum excess pressure of 0.87 MPa, and is a higher fraction when L is smaller. Any sinuosity in the path from the surface to the base, or a smaller value of a/L, would also increase this pressure head loss. Thus, both the $L \ll H$ approximation and the approximation of no loss of excess pressure at the basal inlet are of concern.

For the uniform pressure loading Δp_{in} over a penny-shaped plate of radius L clamped on the edges, *Timoshenko and Woinowsky-Krieger* [1959] gives

$$h_U^P(\mathcal{R}) = \frac{3\Delta p_{in} L^4}{16 E' H^3} (1 - \hat{\mathcal{R}}^2)^2, \quad \text{(D3)}$$

where, as before, $\hat{\mathcal{R}} = \mathcal{R}/L$. The average opening is then

$$\bar{h}_U^P = \frac{1}{16} \cdot \frac{\Delta p_{in} L}{E'} \cdot \frac{L^3}{H^3}. \quad \text{(D4)}$$

Comparing Equation (D4) for $\bar{h}_U^P$, which applies when $L \gg H$, with Equation (53) for $\bar{h}_U^{3D}$, which applies when $L \ll H$, we suggest a summed version of $\bar{h}_U$ (the average opening

under uniform pressure) defined by

$$\bar{h}_U^S \equiv \bar{h}_U^{3D} + \bar{h}_U^P = \frac{16\xi \Delta p_{in} L}{3\pi E'} \left[1 + \frac{3\pi}{256\xi} \cdot \frac{L^3}{H^3} \right]. \quad \text{(D5)}$$

To account for pressure loss in the connecting conduit, we let $\Delta p_{in} \equiv \chi \Delta p_{static}$, where $0 \leq \chi \leq 1$. We then solve for the unknowns χ and U_{vert} (average fluid velocity in the vertical crack) by equating the excess pressures at the juncture between the vertical crack and the basal crack inlet, and similarly equating the volumetric flow rates there. We use the same turbulent scaling as was used in Equation (D2), noting again that this depth-averaged, lumped-parameter treatment of flow in the vertical crack is a crude approximation to the true situation. With this caveat, the first equality is satisfied by

$$(1 - \chi)\Delta p_{static} = \frac{0.0357\rho U_{vert}^2 k^{1/3} H}{(\pi a \chi \Delta p_{static}/2E)^{4/3}}, \quad \text{(D6)}$$

where $\chi \Delta p_{static}$ has replaced Δp_{in}. The second (flow rate) equality is satisfied (as also discussed prior to Equation (D2)) by setting

$$4a u_{avg} U_{vert} = \frac{\pi a^2 \Delta p_{static} U_{vert} \cdot \chi}{E}$$
$$= \frac{dV_b}{dt} = \frac{dV_b}{dL} U_{tip}, \quad \text{(D7)}$$

where U_{tip} is given by Equation (46) and dV_b/dL is calculated as

$$\frac{dV_b}{dL} = C_1 \pi \frac{d(L^2 \bar{h}_U)}{dL}. \quad \text{(D8)}$$

As discussed in the main text, all 3 models (with $\bar{h}_U$, $\bar{h}_U^{3D}$ or $\bar{h}_U^S$) combine a 2D approximation for surface displacements (Equation (50)) with a 3D approximation for volumes (Equation (54)), so all are hybrid models that should not be expected to precisely agree with any realistic situation. Proceeding nonetheless and using 'Model II' (with $\bar{h}_U^{3D}$) in Equation (46), for example, gives

$$U_{tip} = C_2 \sqrt{\frac{\Delta p_{static}}{\rho}} \left(\frac{16\xi \Delta p_{static}}{3\pi E'} \right)^{2/3} \left(\frac{L}{k} \right)^{1/6} \chi^{7/6} \quad \text{(D9)}$$

(where the exponent of $7/6$ on χ comes from $1/2 + 2/3$). Similarly, using 'Model II' in Equation (D8) gives

$$\frac{dV_b}{dL} = \frac{16 C_1 \xi \Delta p_{static}}{3E'} \frac{d(\chi L^3)}{dL}$$
$$= \frac{16 C_1 \xi \Delta p_{static}}{E'} \cdot \chi L^2 (1 + \frac{L}{3\chi} \frac{d\chi}{dL}), \quad \text{(D10)}$$

where it will be shown that the $d\chi/dL$ term can be safely ignored compared with the other term (this is also true for 'Model I', but not for 'Model III'). Using these expressions in Equation (D7), and solving for U_{vert} gives

$$U_{vert} = 4.83 \sqrt{\frac{\Delta p_{static}}{\rho}} \left(\frac{\Delta p_{static}}{E} \right)^{2/3} \left(\frac{L}{k} \right)^{1/6} \left(\frac{L}{a} \right)^2 \cdot \chi^{7/6} \quad \text{(D11)}$$

Substituting U_{vert} into Equation (D6), and ignoring the $d\chi/dL$ term, allows us to solve algebraically for χ in terms of known quantities (and given L and a). Using values from Section 3, then

$$\chi = \frac{(a/L)^{16/3} \cdot (L/H)}{0.456 + (a/L)^{16/3} \cdot (L/H)}. \quad \text{(D12)}$$

Explicitly calculating $d\chi/dL$ with this solution, we find that $(L/3\chi)d\chi/dL \leq 1/3$ regardless of L, and thus small compared to 1, which validates ignoring that contribution in

Equation (D10). If we had used 'Model I' (with $\bar{h}_U$) instead of 'Model II', Equation (D12) would have a numerical factor of 3.55 instead of 0.456, while not changing the rest of the expression. If we instead use 'Model III' (with $\bar{h}_U^S$) instead of 'Model II' to calculate χ, then we can no longer ignore the $d\chi/dL$ term and instead must numerically solve the differential equation to find $\chi(L)$. For plots of χ for these three cases for plausible choices of a/L, see Figure 4.10 of *Tsai* [2009]. For 'Model III' (including approximate plate bending), the strong dependence of U_{tip} on L implies the fast asymptote of $\chi \to 0$ as L grows. This asymptote of $\chi \to 0$ results in the rapid decrease in $\Delta p_{in} \to 0$ and thus rapid closing of the vertical crack which, in turn, is what stabilizes the growth rate of the basal crack. One should note that, in this model, the rapid closing of the vertical crack is complete since it involves a mathematical crack that can close completely under zero excess pressure Δp_{in}, whereas a realistic rough crack would not have complete closure to flow even with $\Delta p_{in} = 0$. The behavior of 'Model III' therefore may be unrealistic.

Finally, in the late stages of crack growth, when the surface lake is gone but there remains excess water pressure driving the basal crack open (with height of liquid water H_w now below the surface height of the glacier H), we assume that the crack system continues to grow while conserving the total water volume in the basal crack plus vertical crack. We now find it convenient to separate the contributions to pressure loss into a hydrostatic component due to $H_w < H$ such that $\Delta p_{hy} \equiv \chi_w \Delta p_{static}$ in hydrostatic equilibrium, and a fractional dynamic component on top of this such that $\Delta p_{in} \equiv \chi \Delta p_{hy} \equiv \chi \cdot \chi_w \Delta p_{static}$. H_w and χ_w can easily be related by expressing hydrostatic balance in terms of H_w, which yields

$$\frac{H_w}{H} = \frac{\rho_{ice}}{\rho} + \frac{\rho - \rho_{ice}}{\rho} \chi_w. \qquad (D13)$$

As expected, when $\chi_w \to 1$, $H_w \to H$ and when $\chi_w \to 0$, $H_w \to 0.91H$. Since the geometric changes in H_w/H are small compared to the effects of χ_w on Δp_{in}, we continue to approximate $H_w \approx H$ when it enters equations geometrically. With this approximation, we then find that χ is still determined by Equation (D12). Maintaining $V_b + V_c = V_0$ in 'Model II' (i.e., using Equation (D1) implemented with $\bar{h}_U^{3D}$) then determines $\chi_0 \equiv \chi\chi_w$ to be

$$\chi_0 = \frac{EV_0}{\pi \Delta p_{static} L^3} \cdot \frac{L/H}{0.503 L/H + (a/L)^2}. \qquad (D14)$$

Thus, $\Delta p_{in}/\Delta p_{static} \equiv \chi_0$ is again determined algebraically as a function of L (and a/L) during the late stages of basal crack growth.

Notation

A	constant related to U_{tip} in Eq. (13).
A'	constant related to A.
A_k	self-similar series constants.
a	half length of connecting conduit.
b	distance along crack of force pair.
C_1	$h_{avg}/\bar{h}_U$.
C_2	scaling factor for velocity in Eq. (46).
c_0	coefficient in lubrication equation.
c_k	constants chosen to satisfy $K_{Ic} = 0$.
D	self-similar series constant.
D^*	size of largest entrained grains.
E	Young's modulus.
E'	effective modulus in plane strain.
E_{loss}	energy loss.
e_{loss}	energy loss per unit area.
F_{ij}	angular function associated with σ_{ij}.
$F(\hat{x})$	pressure term associated with first term of self-similar opening series.
f	Darcy-Weisbach friction factor.
f_0	value of f at reference scale.
G	shear modulus.
g	gravitational acceleration.
$g(z), F(z)$	complex bimaterial functions.
H	height of ice sheet.
H_w	height of water.
h	basal crack opening.
h_0	crack opening estimate.
h_{avg}	average value of h.
h_s	surface uplift from crack opening.
h_s^V	surface uplift from V_c crack.
h_U^P	opening of plate for uniform p.
$\bar{h}_U$	average opening for uniform p.
$\bar{h}_U^{3D}$	average opening for 3D uniform p.
$\bar{h}_U^P$	average opening of plate for uniform p.
$\bar{h}_U^S$	average opening of 3D crack plus plate.
I_k	integral expressions.
K_I	stress intensity factor.
K_{Ic}	fracture toughness.
k	Nikuradse roughness height.
L	horizontal basal crack length.
$\hat{L}$	non-dimensional L.
L_0	characteristic scale for L.
L_c	surface crack length.
LHS	left-hand side of Eq. (26).
l	conductive length scale.
m	power-law index.
n	Manning roughness.
P	constant in Eq. (13).
p	fluid pressure in crack.
Δp	pressure in excess of hydrostatic.
$\hat{p}$	non-dimensional Δp.
Δp_0	characteristic scale for Δp.
Δp_{in}	excess pressure at crack inlet.
Δp_{hy}	hydrostatic component of Δp_{in}.
Δp_{static}	Δp from column of standing water.
Δp_{loss}	loss of pressure in excess of hydrostatic.
Q_{2D}	2D flow rate.
Q_b	flow rate contributed by V_b.
Q_c	flow rate contributed by V_c.
q	constant in complex potential.
R	distance along crack behind crack tip.
$\mathcal{R}$	distance from center of 3D crack.
$\hat{\mathcal{R}}$	non-dimensional $\mathcal{R}$.
R_h	hydraulic radius.
$\Re$	Reynolds number.
RHS	right-hand side of Eq. (26).
r	distance away from crack tip.
S	negative hydraulic head gradient.
$s, \hat{s}$	dummy variables.
T	timescale of drainage.
t	time.
$\hat{t}$	non-dimensional t.
U	fluid velocity averaged across h.
$\hat{U}$	non-dimensional U.

U_0	characteristic scale for U.
$U_{Manning}$	Manning velocity.
U_{vert}	average velocity in vertical conduit.
U_{tip}	crack-tip velocity.
u_{P1}	horizontal displacement due to force pair.
u_s	surface horizontal displacement.
$u + iv$	complex displacement.
V_0	initial lake volume.
V_{2D}	2D crack volume.
V_b	basal crack volume.
V_c	connecting crack volume.
W_L	water level.
w	model crack opening.
$\hat{w}$	non-dimensional w.
w_0	characteristic scale for w.
w_k	terms of self-similar opening series.
w_U	model opening for uniform p.
w_U^{3D}	model opening of 3D crack for uniform p.
x	horizontal position along crack.
x_0	horizontal sensor position.
y	vertical position.
z	complex variable.
α, β, γ	self-similar constants.
$\dot{\gamma}$	shear rate.
δ	elastic constant relating w and Δp.
ϵ	bimaterial mismatch constant.
ϵ_m	normalized squared error.
η	water viscosity.
η_k	$3 - 4\nu_k$.
ϕ	self-similar constant for velocity scale.
φ	dummy variable.
$\phi(z), \psi(z)$	Muskhelishvili potentials.
κ	thermal diffusivity.
ν, ν_k	Poisson's ratio.
ρ	water density.
ρ_{ice}	ice density.
ρ_s	grain density.
σ_0	hydrostatic ice overburden pressure.
σ_{ij}	stress tensor components.
τ	average shear stress on channel walls.
τ_{b0}	initial basal shear stress.
τ_c^*	dimensionless critical Shields stress.

τ_d	diffusion timescale.
θ	angle around crack tip.
ξ	h/w.
χ	$\Delta p_{in}/\Delta p_{hy}$.
χ_w	$\Delta p_{hy}/\Delta p_{static}$.
χ_0	$\chi \cdot \chi_w$.

References

Das, S., I. Joughin, M. D. Behn, I. M. Howat, M. A. King, D. Lizarralde, and M. P. Bhatia (2008), Fracture propagation to the base of the Greenland Ice Sheet during supraglacial lake drainage, *Science*, *320*, doi:10.1126/science.1153360.

Desroches, J., E. Detournay, B. Lenoach, P. Papanastasiou, J. R. A. Pearson, M. Thiercelin, and A. Cheng (1994), The crack tip region in hydraulic fracturing, *Proc. R. Soc. Lond. A*, *447*, 39–48.

England, A. H. (1965), A crack between dissimilar media, *J. App. Mech.*, *32*, 400–402.

Erdogan, F. (1965), Stress distribution in bonded dissimilar materials with cracks, *J. App. Mech.*, *32*, 403–410.

Lay, T., and T. C. Wallace (1995), *Modern Global Seismology*, 521 pp., Academic Press, San Diego.

Muskhelishvili, N. I. (1953), *Some Basic Problems of the Mathematical Theory of Elasticity*, 3rd ed., 704 pp., Noordhoff Ltd, Groningen, Holland.

Rice, J. R., and G. C. Sih (1965), Plane problems of cracks in dissimilar media, *J. App. Mech.*, *32*, 418–423.

Tada, H., P. C. Paris, and G. R. Irwin (2000), *The Stress Analysis of Cracks Handbook*, 3rd ed., 677 pp., ASME Press, New York.

Timoshenko, S., and S. Woinowsky-Krieger (1959), *Theory of Plates and Shells*, 2nd ed., 580 pp., McGraw-Hill, New York.

Timoshenko, S. P., and J. N. Goodier (1987), *Theory of Elasticity*, 3rd ed., 567 pp., McGraw-Hill, New York.

Tsai, V. C. (2009), The use of simple physical models in seismology and glaciology, Ph.D. thesis, Harvard University.

Walsh, J. B., and J. R. Rice (1979), Local changes in gravity resulting from deformation, *J. Geophys. Res.*, *84*, 165–170.

V. C. Tsai, Department of Earth and Planetary Sciences, Harvard University, 20 Oxford St., Cambridge, MA 02138, USA. (vtsai@post.harvard.edu)

J. R. Rice, Department of Earth and Planetary Sciences and School of Engineering and Applied Sciences, Harvard University, 29 Oxford St., Cambridge, MA 02138, USA. (rice@seas.harvard.edu)